J. Fluid Mech. (1999), *vol.* 391, *pp.* 211–247. Printed in the United Kingdom

A DNS-based thermal second-moment closure for buoyant convection at vertical walls

By H. S. DOL, K. HANJALIĆ† AND T. A. M. VERSTEEGH

Applied Physics Department, Delft University of Technology, PO Box 5046, 2600 GA Delft, The Netherlands

(Received 23 March 1998 and in revised form 19 February 1999)

Direct numerical simulations (DNS) of natural convection in a vertical channel by Versteegh & Nieuwstadt (1998) are used for assessing the budget of the turbulent heat flux $\overline{\theta u_i}$ and the temperature variance $\overline{\theta^2}$, and for modelling the transport equations governing these two properties. The analysis is confined to a simple fully developed situation in which the gravitational vector, as the sole driving force, is perpendicular to the only non-zero component of the mean temperature gradient. Despite its simplicity, the flow displays many interesting features and represents a generic case of the interaction of buoyancy-driven turbulent temperature and velocity fields. The paper discusses the near-wall variation of the second moments and their budgets, as well as possible scaling of $\overline{\theta u_i}$ and $\overline{\theta^2}$ both in the near-wall region and away from the wall. Various proposals for the Reynolds-averaged modelling are analysed and new models are proposed for these two transport equations using the term-by-term approach. An *a priori* test (using the DNS data for properties other than $\overline{\theta u_i}$ and $\overline{\theta^2}$) reproduced very well all terms in the transport equations, as well as their near-wall behaviours and wall limits, without the use of any wall-topology-dependent parameters. The computational effort is still comparable to that for the 'basic model'. The new term-by-term model of the $\overline{\theta u_i}$ and $\overline{\theta^2}$ equations was then used for a full simulation in conjunction with a low-Reynolds-number second-moment velocity closure, which was earlier found to reproduce satisfactorily a variety of isothermal wall flows. Despite excellent term-by-term reproduction of thermal turbulence, the predictions with the full model show less satisfactory agreement with the DNS data than *a priori* validation, indicating a further need for improvement of the modelling of buoyancy effects on mechanical turbulence.

1. Introduction

One-point Reynolds-averaged Navier–Stokes (RANS) turbulence closures serve currently as a basis of applied computational fluid dynamics (CFD). Despite noted deficiencies, RANS models are used widely for computation of complex flows and transport processes in various branches of industry. A continuous increase in computing power stimulates further efforts towards improvement of the models, allowing greater model complexity while maintaining the computational costs within affordable limits. New incentive comes from direct numerical simulations (DNS), which provide

† Author to whom correspondence should be addressed.

information (albeit only for simple flow domains and at low Reynolds and Rayleigh numbers) about the terms in averaged transport equations that are inaccessible to any available measuring techniques.

Extensive validation over the past decade in an increasing variety of flows has enabled a better distinction between the potential of various models. It is generally recognized that the two-equation k-ε eddy-viscosity models with linear stress–strain relations and their analogue for scalar fields cannot reproduce any flows with significant non-equilibrium effects, flows subjected to body forces or to any extra-strain rates other than simple shear. In flows driven purely by thermal buoyancy, deficiencies of isotropic eddy-diffusivity models by which the turbulent heat flux is expressed in terms of the aligned component of the mean temperature gradient, are even more transparent. For example, in a mixed layer heated from below, the major turbulent heat flux in the vertical direction has no relation with the typically uniform mean temperature. Likewise, in a boundary layer along a heated vertical wall the major source of buoyancy-induced turbulence originates from the substantial vertical heat flux, while the temperature gradient in the vertical direction is usually small or negligible. These deficiencies can be cured by adopting the second-moment closure level, either by solving in differential form the transport equations for second moments, or as a basis for deriving truncated models in the form of algebraic expressions for turbulent stress and scalar flux.

However, while inevitably more complex and computationally more demanding, there is a view among the CFD community that these models have not fulfilled the early expectation in demonstrating indisputable superiority over simpler two-equation k-ε and similar models. DNS have also revealed how poorly most current closures, including the second-moment ones, reproduce individual budget terms, even if the mean flow properties are predicted well in accord with those obtained by DNS or experiments. Because of these and other failures, there is a view that one-point closures should be abandoned and replaced by the large-eddy simulation (LES) technique as the future industrial computational tool. While such prospects may be realistic for specific types of flows dominated by large eddy structures away from solid walls, a wider application of LES to high-Reynolds-number flows in complex, wall-bounded domains seems still distant. The same applies to buoyancy-driven flows at high Rayleigh numbers, particularly in cases where the wall heat transfer is the major prediction objective. The one-point RANS approach will remain for some time the only viable means for complex industrial computations. Of course, improvements are needed and possible, and this article outlines some prospects in that direction, with a focus on buoyancy-driven flows and heat transfer along vertical walls.

It has been recognized that the second-moment closure models offer a sounder framework for reproducing more accurately the turbulence dynamics and mean flow properties. A major advantage is the possibility for exact treatment of some important turbulence interactions (e.g. stress production, effects of rotation, buoyancy) or for a sounder modelling of the remaining terms by introducing a stress/flux-anisotropy parameter. However, higher-order models do not give *a priori* decisive advantages and more reliable predictions in every flow situation. Because of a need to model many more terms, the second-moment closures bring in more uncertainty and possibilities for ill-founded and unrealistic models of specific interactions, which can annul the natural advantages of the method. This is particularly the case for flows governed by thermal buoyancy, for which the second-moment closures contain a large number of terms which need to be modelled and for which scarce experimental and DNS data are available. Because of this, relatively little effort has been put into the development

of second-moment turbulence closure models that are suited for the thermal field, especially when the flow is driven solely by thermal buoyancy.

Besides, buoyant flows are characterized by some specific features which cannot be described by simple extrapolation of modelling principles, used for non-buoyant turbulent flows. An example is the departure from local energy equilibrium both in physical and spectral space. The large-scale coherent structures which govern the turbulent transport e.g. in fluids heated from below, may generate a true (Boudjemadi *et al.* 1997; Versteegh & Nieuwstadt 1998) or apparent (Kenjereš & Hanjalić 1995) counter-gradient diffusion, or may emphasize the role of pressure diffusion as discovered by DNS in Rayleigh–Bénard convection (Wörner & Grötzbach (1997). Buoyancy produces a unidirectional stratification and, depending on the orientation of the temperature-gradient vector imposed by the boundary conditions with respect to the gravitation vector, a variety of regimes may coexist in a single flow domain even at relatively high bulk-Rayleigh numbers, ranging from stagnant fluid to laminar circulation, the transitional regime and fully turbulent regions. This emphasizes the role of molecular effects both close to a solid boundary and away from walls (at the edge of turbulent flows) and the need to use models which can universally account for low-Reynolds- and Péclet-number phenomena, irrespective of the wall vicinity. On the other hand, strong variation of all flow properties in usually very thin boundary layers along the walls, where the buoyancy has the strongest effects on turbulence, requires a fine numerical resolution of the near-wall region and adequate modelling of both the viscous and conduction effects as well as non-viscous, non-conductive wall-blockage effects. To this one may add also a lack of universal scaling for different boundary conditions (orientation of heated walls) which hampers any prospects for computational bridging of the near-wall regions.

This study is aimed at assessing the current practice in modelling various terms in the transport equation for the turbulent heat flux and temperature variance. It also contributes towards the modelling of turbulent natural convection by presenting a new differential thermal second-moment closure. The unclosed terms that appear in the transport equations for the turbulent heat flux $\overline{\theta u_i}$ and temperature variance $\overline{\theta^2}$ are remodelled using the results of DNS of natural convection in a vertical channel (Versteegh & Nieuwstadt 1998) and the asymptotic analysis of turbulence velocity and temperature correlations in the near-wall region. The analysis is confined to vertical heated walls. For complementary DNS-based modelling of Rayleigh–Bénard convection, the reader is referred to recent papers by Girimaji & Balachandar (1997), Wörner & Grötzbach (1997) and Ye *et al.* (1997).

The proposed model requires a fine grid near the wall, which may still hinder its wider application to very complex three-dimensional flows at high Reynolds numbers. It is argued, however, that this approach may be unavoidable if wall heat transfer is the focus. Successful reproduction of the near-wall second-moment statistics (in addition to mean flow) qualifies this approach (in full or a truncated form) either for steady or transient RANS computations. It can also serve as a basis for developing a near-wall subgrid-scale model for LES, or for hybrid RANS/LES computations, which are regarded as a promising route to predicting complex wall-bounded flows.

2. Flow specification, governing equations and methods of solution

Natural convection in a vertical channel is driven entirely by the thermal buoyancy generated by the temperature difference between the opposing walls. Figure 1(*a*) shows the flow geometry considered. The two flat walls of the channel are separated

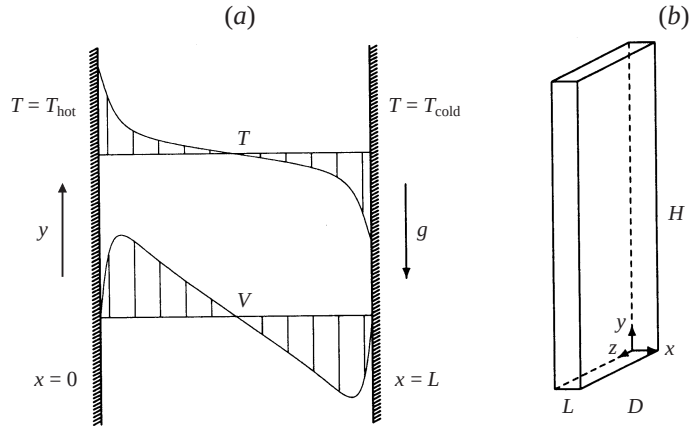

FIGURE 1. A schematic representation of the vertical-channel set-up (*a*) and the three-dimensional box used for the direct numerical simulations (*b*).

by a distance L in the x-direction and extend indefinitely in the y- and z-directions. Both walls are isothermally heated at fixed but different temperatures. The gravitation vector g_i is aligned with the walls and points downwards in the negative y-direction. Buoyancy will force the flow upwards along the hot wall and downwards along the cold wall. The vertical boundary layers are completely mixed (no stably stratified core region) and the flow is fully developed and anti-symmetric with respect to the mid-plane, which simplifies the numerical simulation.

The equations that describe the instantaneous (marked with primes) velocity and temperature field are the unsteady three-dimensional momentum, continuity and energy equations:

$$\frac{\partial U_k'}{\partial x_k} = 0, \tag{2.1}$$

$$\frac{\mathrm{D}U_i'}{\mathrm{D}t} = -\frac{1}{\rho}\frac{\partial P'}{\partial x_i} + \nu\frac{\partial^2 U_i'}{\partial x_k^2} - g_i\beta(T' - T_{\mathrm{ref}}), \tag{2.2}$$

$$\frac{\mathrm{D}T'}{\mathrm{D}t} = \alpha\frac{\partial^2 T'}{\partial x_k^2}, \tag{2.3}$$

where $\mathrm{D}/\mathrm{D}t = \partial/\partial t + U_k'\partial/\partial x_k$ denotes the material derivative and the indices $i = 1, 2, 3$ correspond to the x-, y- and z-directions, respectively. Other symbols have the standard meaning: ρ is the fluid density, ν is the kinematic viscosity, β is the thermal expansion coefficient and α is the thermal diffusivity. The Boussinesq approximation has been applied, which has little consequence at moderate temperature differences for fluids with Prandtl numbers close to unity. The boundary conditions at the walls are $U_i' = 0$, $T' = T_{\mathrm{hot}}$ (left wall) and $T' = T_{\mathrm{cold}}$ (right wall). The reference temperature T_{ref} can be chosen arbitrarily and the average temperature $T_{\mathrm{av}} = (T_{\mathrm{hot}} + T_{\mathrm{cold}})/2$ is a common choice. The pressure P' in equation (2.2) actually is the reduced pressure, i.e. relative to the hydrostatic pressure $P_0 + \rho g_k x_k$.

The DNS was performed by solving equations (2.1)–(2.3) numerically in time and space for a three-dimensional box such as depicted in figure 1(*b*). Periodic boundary conditions were applied at the domain boundaries in the y- and z-directions, at sufficiently large height H and depth D for the correlation between the opposing periodic boundaries to be negligibly small. Once available, the DNS enables the

statistics of the flow (mean velocity, mean temperature, second and higher moments) to be uniquely obtained by ensemble averaging a large number of realizations. In the computation, the ensemble average is replaced by space averaging in the homogeneous directions and/or time averaging over intervals much larger than the typical eddy-turnover time and much smaller than time scales imposed by the boundary conditions. A necessary condition is that the flow is statistically stationary and fully turbulent. Versteegh & Nieuwstadt (1998) applied space averaging in the homogeneous y, z-directions and time averaging.

DNS is at present the only method that can provide reliable information about the instantaneous velocity, pressure and temperature field. However, because the smallest time and length scales of the turbulence need to be resolved, DNS poses high demands on available computer resources, especially at high Reynolds and Rayleigh numbers and when the turbulence intensity and anisotropy is large. For more complex flows of industrial relevance, the solution of modelled transport equations for the statistics themselves offers a more rational route than the DNS approach. The conventional splitting into the mean and fluctuation part ($U_i' = U_i + u_i$, $T' = T + \theta$, $P' = P + p$) and ensemble averaging yields the following set of RANS equations for mean velocity U_i and temperature T:

$$\frac{\partial U_k}{\partial x_k} = 0, \tag{2.4}$$

$$\frac{\mathrm{D}U_i}{\mathrm{D}t} = -\frac{1}{\rho}\frac{\partial P}{\partial x_i} + \nu\frac{\partial^2 U_i}{\partial x_k^2} - g_i\beta(T - T_{\mathrm{ref}}) - \frac{\partial \overline{u_i u_k}}{\partial x_k}, \tag{2.5}$$

$$\frac{\mathrm{D}T}{\mathrm{D}t} = \alpha\frac{\partial^2 T}{\partial x_k^2} - \frac{\partial \overline{\theta u_k}}{\partial x_k}, \tag{2.6}$$

where the second moments, the turbulent-stress tensor $\overline{u_i u_k}$ and heat-flux vector $\overline{\theta u_k}$, which appear as a consequence of the loss of information due to averaging, need to be modelled. This constitutes the primary objective of the present study. The adopted level of modelling is the differential second-moment closure. In comparison to the turbulent stress, relatively little has been published about the closure of the equation for the turbulent heat flux, especially when temperature is not a passive scalar. Therefore, we limit at present our scope to modelling the turbulent heat flux, with the use of DNS data.

Earlier attempts in this direction were based on experiments, which provided only a limited amount of information at a limited number of locations. The DNS data provide all the information needed for term-by-term modelling of the second-moment transport equations. For an isothermal channel flow, the potential of such an approach has already been convincingly demonstrated by Mansour, Kim & Moin (1988). Here, a similar exercise will be performed for natural-convection channel flow.

In devising the models, we aim at matching the DNS data as closely as possible, while keeping the model relatively simple. Primarily, the effort is focused on accurate near-wall modelling with full compliance with the mathematical constraints, such as coordinate-transformation invariance, the two-component limit and realizability, while eliminating the use of surface-topology parameters.

2.1. *The DNS database*

Several sets of DNS results for turbulent buoyant convection that have appeared recently provide missing information which is inaccessible to experimental techniques. Comprehensive data sets now available enable a deeper insight into the physics of

such flows and an evaluation of the current modelling practice. They also provide an incentive for deriving better models based on a more rigourous analysis of the flow physics. Although most of the studies are confined to two basic cases, i.e. Rayleigh–Bénard convection between two infinite horizontal plates heated from below (Grötzbach 1982; Balachandar, Maxey & Sirovich 1989) and the flow between two differentially heated vertical plates (Boudjemadi *et al.* 1997; Versteegh & Nieuwstadt 1998), these data enable a comparative study and model validation in two generic situations in which the gravitational vector is either parallel or perpendicular to the mean-temperature-gradient vector. DNS results are available also for more complex cases such as turbulent natural convection in differentially heated cavities with adiabatic upper and lower walls (two-dimensional simulations by Paolucci 1990, and a three-dimensional case by Henkes & Le Quéré 1996), though at relatively low Rayleigh numbers and focusing mainly on flow development and transition.

In this study, we consider only the thermal convection between vertical infinite plates. The data of Versteegh & Nieuwstadt (1998) have been used for reference. These seem more accurate than the results of Boudjemadi *et al.* (1997), because the latter authors used a smaller solution domain both in the vertical and spanwise direction. The flow is characterized by the Prandtl number $Pr = \nu/\alpha = 0.709$ and the Rayleigh number $Ra = g\beta\Delta T L^3 Pr/\nu^2 = 5.4 \times 10^5$, 8.227×10^5, 2×10^6 and 5×10^6, corresponding to turbulent air flow at four different values of the temperature difference. The smallest and the largest Rayleigh numbers differ by approximately one decade. The aspect ratios of the computational box (see figure 1*b*) are $H/L = 12$ (height over width) and $D/L = 6$ (depth over width).

The DNS were performed using a standard finite-volume method with second-order discretization schemes (Versteegh & Nieuwstadt 1998). With the application of Richardson extrapolation on two grids, which differ by approximately a factor two, the solutions were obtained with approximately fourth-order accuracy. The highest grid resolution was taken to be $N_x \times N_y \times N_z = 96 \times 432 \times 216$. The distance between the grid points is non-uniform in the x-direction, with the smallest grid cell near the walls ($\Delta x_{\min}/L = 4.39 \times 10^{-3}$) and the largest grid cell in the centre of the channel ($\Delta x_{\max}/L = 1.31 \times 10^{-2}$). The grid in the other two (homogeneous) coordinate directions is uniform. The grid resolution was high enough to resolve the Kolmogorov microscales at $Ra = 8 \times 10^5$, in compliance with the criterion proposed by Grötzbach (1983). More details are provided by Versteegh (1998). The DNS database provides all statistics as a function of x/L, interpolated on a *uniform* grid consisting of 200 (internal) grid points. The data include all first, second and third moments of velocity and temperature and all budget terms of the Reynolds stress, turbulent heat flux and temperature variance. The pressure terms in the budgets are first decomposed into pressure transport and the pressure-scrambling correlations, which are further decomposed into slow, rapid, buoyant and wall parts. The data have been non-dimensionalized using the length scale L, the buoyant velocity scale $V_b = (g\beta\Delta T L)^{1/2}$ and the temperature scale ΔT.

The analysis of the DNS data revealed some specific features which have been the subject of controversy. Because of the multiple mechanisms by which the turbulent stress and heat flux are generated (mean rate of strain, buoyancy, mean temperature gradient), the conventional stress–strain or flux–mean-temperature-gradient relations as implied by the eddy-viscosity/diffusivity hypotheses are inappropriate. It is noted that all three sources are of the same order of magnitude. The mean-shear turbulence generation is negative close to the wall for all second moments, changing its sign around the mean velocity maximum, whereas all stress and flux components are

everywhere positive except for a very small (almost negligible) negative value of the shear stress very close to the wall. These features emphasize the need to employ the second-moment closure approach as a minimum modelling level. The pressure scrambling is the dominant sink of the turbulent heat flux, whereas the molecular dissipation is negligible, except close to the wall where it balances molecular transport. Another interesting feature, contrary to for example the stress budget in a plane channel or a plane Couette flow, is that the return-to-isotropy (slow) term is the dominant constituent of the pressure-scrambling process for all heat-flux components as well as for all stresses. The exception is the shear stress where the rapid term exceeds all others in the pressure-scrambling term. The dominance of the nonlinear (slow) term can be attributed to large relative fluctuations of temperature and velocity, as compared for example with a forced, shear-dominated convection in a similar configuration.

3. Term-by-term modelling of the thermal equations

The exact equation for the turbulent heat flux $\overline{\theta u_i}$ is:

$$\frac{\mathrm{D}\overline{\theta u_i}}{\mathrm{D}t} = \underbrace{\frac{\partial}{\partial x_k}\left[\underbrace{\boxed{\alpha\overline{\frac{\partial\theta}{\partial x_k}u_i} + \nu\theta\overline{\frac{\partial u_i}{\partial x_k}}}}_{\mathscr{D}^{\mathrm{v}}_{\theta i}} \underbrace{\boxed{-\overline{\theta u_i u_k}}}_{\mathscr{D}^{\mathrm{t}}_{\theta i}}\right]}_{\mathscr{D}_{\theta i}} \underbrace{-\overline{u_i u_k}\frac{\partial T}{\partial x_k}}_{P^{\mathrm{th}}_{\theta i}}$$
$$\underbrace{-\overline{\theta u_k}\frac{\partial U_i}{\partial x_k}}_{P^{\mathrm{m}}_{\theta i}} \underbrace{\boxed{-g_i\beta\overline{\theta^2}}}_{G_{\theta i}} \underbrace{\boxed{-\overline{\frac{\theta}{\rho}\frac{\partial p}{\partial x_i}}}}_{\Pi_{\theta i}} - \underbrace{\boxed{(\alpha+\nu)\overline{\frac{\partial\theta}{\partial x_k}\frac{\partial u_i}{\partial x_k}}}}_{\varepsilon_{\theta i}}. \qquad (3.1)$$

The material derivative is zero in the present case and the terms on the right-hand side of the equation are the viscous diffusion $\mathscr{D}^{\mathrm{v}}_{\theta i}$, turbulent diffusion $\mathscr{D}^{\mathrm{t}}_{\theta i}$, thermal production $P^{\mathrm{th}}_{\theta i}$, mechanical production $P^{\mathrm{m}}_{\theta i}$, buoyant production $G_{\theta i}$, temperature–pressure-gradient correlation ('pressure scrambling') $\Pi_{\theta i}$ and the dissipation rate $\varepsilon_{\theta i}$. The terms in boxes have to be modelled. The only unknown correlation in equation (3.1) for which another transport equation is solved, is the temperature variance $\overline{\theta^2}$. The exact equation for $\overline{\theta^2}$ is

$$\frac{\mathrm{D}\overline{\theta^2}}{\mathrm{D}t} = \underbrace{\frac{\partial}{\partial x_k}\left[\underbrace{\alpha\frac{\partial\overline{\theta^2}}{\partial x_k}}_{\mathscr{D}^{\mathrm{v}}_{\theta\theta}} \underbrace{\boxed{-\overline{\theta^2 u_k}}}_{\mathscr{D}^{\mathrm{t}}_{\theta\theta}}\right]}_{\mathscr{D}_{\theta\theta}} \underbrace{-2\overline{\theta u_k}\frac{\partial T}{\partial x_k}}_{P_{\theta\theta}} - \underbrace{\boxed{2\alpha\overline{\frac{\partial\theta}{\partial x_k}\frac{\partial\theta}{\partial x_k}}}}_{\varepsilon_{\theta\theta}}. \qquad (3.2)$$

The budget terms can be assigned a physical meaning analogous to that above: viscous diffusion $\mathscr{D}^{\mathrm{v}}_{\theta\theta}$, turbulent diffusion $\mathscr{D}^{\mathrm{t}}_{\theta\theta}$, production $P_{\theta\theta}$ and dissipation $\varepsilon_{\theta\theta}$.

3.1. *Wall limits*

It is known that a solid wall exerts a strong effect on the turbulence both by viscous and non-viscous suppression of turbulence fluctuations. While the viscous

i	1	2	θ
$\mathscr{D}^{v}_{\theta i}$	$2(\alpha+2\nu)\overline{b_\theta c_1}x$	$\boxed{(\alpha+\nu)\overline{b_\theta b_2}}$	$\boxed{2\alpha\overline{b_\theta^2}}$
$\hat{\mathscr{D}}^{v}_{\theta i}$	$3(\alpha+\nu)\overline{b_\theta c_1}x$	$\boxed{(\alpha+\nu)\overline{b_\theta b_2}}$	
$\mathscr{D}^{p}_{\theta i}$	$\boxed{-(1/\rho)\overline{b_\theta a_p}}-(2/\rho)(\overline{b_\theta b_p}+\overline{c_\theta a_p})x$		
$\Phi_{\theta i}$	$\boxed{(1/\rho)\overline{b_\theta a_p}}+(1/\rho)(\overline{b_\theta b_p}+2\overline{c_\theta a_p})x$	$(1/\rho)(\overline{\partial b_\theta/\partial y)a_p}x$	
$\Pi_{\theta i}$	$-(1/\rho)\overline{b_\theta b_p}x$	$(1/\rho)(\overline{\partial b_\theta/\partial y)a_p}x$	
$\varepsilon_{\theta i}$	$2(\alpha+\nu)\overline{b_\theta c_1}x$	$\boxed{(\alpha+\nu)\overline{b_\theta b_2}}$	$\boxed{2\alpha\overline{b_\theta^2}}$

TABLE 1. Near-wall behaviour of viscous diffusion, pressure terms and dissipation (leading terms of their Taylor-series expansions). Note: terms in boxes are in balance at the wall. Models are denoted with the 'hat' symbol.

effect is of a scalar nature, the non-viscous effect due to blockage (impermeability, pressure reflection) is dependent on the wall proximity and configuration. In the flow over heated walls the near-wall turbulence is further affected because the flow is driven by the imposed wall conditions. As no universal scaling of flow properties has been established for any class of flows driven by thermal buoyancy, prospects for deriving wall functions for bridging the viscous and conductive layers are slim. Consequently, the equations have to be integrated up to the wall with appropriate low-Re_t and non-viscous modifications. Modelling the wall effect is one of the prime difficulties, but it is a crucial prerequisite for the simulation of flow properties near walls, especially for the prediction of wall friction and heat transfer. It follows from the DNS data that the Nusselt number $Nu = -(L/\Delta T)(\mathrm{d}T/\mathrm{d}x)_w$ scales with approximately $Ra^{1/3}$, which is a well-known engineering value ($Ra^{1/4}$ for laminar flow). Also, $c_f = (\nu/V_b^2)(\mathrm{d}V/\mathrm{d}x)_w \propto Ra^{1/4}$ appears to be a reasonable assumption for the friction coefficient.

Satisfying the limiting behaviour of the models at the wall is one of the basic requirements of near-wall modelling. Expressions for the wall limits of all budget terms can be derived by substituting Taylor-series expansions for the flow variables. The pressure, velocity and temperature fluctuations can be expanded as follows:

$$p = a_p + b_p x + c_p x^2 + d_p x^3 + \cdots, \tag{3.3}$$

$$u_i = a_i + b_i x + c_i x^2 + d_i x^3 + \cdots, \tag{3.4}$$

$$\theta = a_\theta + b_\theta x + c_\theta x^2 + d_\theta x^3 + \cdots, \tag{3.5}$$

with $a_i = b_1 = a_\theta = 0$ (no-slip condition, continuity and constant wall temperature). The expansions for $\overline{\theta u_i}$ and $\overline{\theta^2}$ then become, in a vertical channel,

$$\overline{\theta u} = \overline{b_\theta c_1}x^3 + (\overline{b_\theta d_1} + \overline{c_\theta c_1})x^4 + \cdots, \tag{3.6}$$

$$\overline{\theta v} = \overline{b_\theta b_2}x^2 + (\overline{b_\theta c_2} + \overline{c_\theta b_2})x^3 + (\overline{b_\theta d_2} + \overline{c_\theta c_2} + \overline{d_\theta b_2})x^4 + \cdots, \tag{3.7}$$

$$\overline{\theta^2} = \overline{b_\theta^2}x^2 + 2\overline{b_\theta c_\theta}x^3 + (2\overline{b_\theta d_\theta} + \overline{c_\theta^2})x^4 + \cdots. \tag{3.8}$$

Similar expressions can be derived for the budget terms, of which only the leading

origin:	$\overline{\theta u}$	$\mathscr{D}^{v}_{\theta 1}$	$\hat{\mathscr{D}}^{v}_{\theta 1}$	$\mathscr{D}^{p}_{\theta 1}$, $\Phi_{\theta 1}$	$\Pi_{\theta 1}$	$\varepsilon_{\theta 1}$
$\overline{b_\theta c_1}$:	(177.3)	75.47	74.76			73.50
$(1/\rho)\overline{b_\theta a_p}$:				−0.06262		
$(1/\rho)\overline{b_\theta b_p}$:	(0.4063)	0.1730	0.1713		0.1913	0.1684
$(1/\rho)\overline{c_\theta a_p}$:				−0.04592		

origin:		$\overline{\theta v}$	$\mathscr{D}^{v}_{\theta 2}$, $\hat{\mathscr{D}}^{v}_{\theta 2}$, $\varepsilon_{\theta 2}$	$\Phi_{\theta 2}$, $\Pi_{\theta 2}$	$\overline{\theta^2}$	$\mathscr{D}^{v}_{\theta\theta}$, $\varepsilon_{\theta\theta}$
$\overline{b_\theta b_2}$:		1.726	1.771			
$(1/\rho)(\overline{\partial b_\theta/\partial y)a_p}$:				−0.2680		
$\overline{b_\theta^2}$:					10.18	10.16

TABLE 2. Values of the correlations (one in each row), appearing in table 1, at $Ra = 5.4 \times 10^5$. Depending on the number of independent origins (one in each column) one or more values are given.

terms are listed in table 1. The budget terms that are at least of second order in x are omitted as their wall limits are considered to be less important. For illustration and further discussion the wall limits are also shown for $\Phi_{\theta i} = \overline{(\partial\theta/\partial x_i)p}/\rho$ and $\mathscr{D}^{p}_{\theta i} = -(\partial\overline{\theta p}/\partial x_i)/\rho$, the sum of which yields the total pressure scrambling $\Pi_{\theta i}$.

The unknown correlations that appear in table 1 can be extracted from the DNS data. The correlations $\overline{b_\theta a_p}/\rho$, $\overline{b_\theta b_2}$ and $\overline{b_\theta^2}$ are directly available through the wall values of the budget terms in which they appear. The other correlations have to be determined from the near-wall slopes of the corresponding budget terms. These slopes are shown in figure 2 for $Ra = 5.4 \times 10^5$. The turbulent heat flux and the temperature variance are also included. The solid lines indicate x^n proportionalities, with $n = 1$, 2 and 3. Table 2 contains the dimensionless values of all correlations from table 1 at $Ra = 5.4 \times 10^5$, with the origins indicated. Here the relationship $\overline{b_\theta b_p}/\rho = 2\nu\overline{b_\theta c_1}$ has been used, which follows from the balance of terms of first order in x for $i = 1$. When deriving the values of correlations, the x^n proportionality was assumed to be valid exactly. This means that if the DNS data show a proportionality x^r, with r slightly smaller than n, the resulting value of the correlation is slightly too large. For $n = 3$, the deviation is particularly significant. Consequently, the values derived from $\overline{\theta u}$ are placed between brackets in table 2. It should be pointed out, however, that the deviation is restricted to the data points nearest to the wall. These errors are, like the scatter in the remaining values, probably caused by the Richardson-extrapolation technique (which applies polynomial curve fitting) and the relative coarseness of the uniform grid near the wall.

In figure 3(*a*), the values from table 2 (except those between brackets) are displayed, together with the values at $Ra = 8.227 \times 10^5$, 2×10^6 and 5×10^6. The figure shows the Rayleigh-number dependence of the correlations with the present non-dimensionalization. In an attempt to reduce the Rayleigh-number dependence, we have replaced the lengthscale L by LRa^a, the velocity scale V_b by $V_b Ra^b$ and the temperature scale ΔT by $\Delta T Ra^c$. Taking a linear least-squares fit with a singular-value decomposition and discarding the extremely deviating value of $\overline{b_\theta b_2}$ at $Ra = 5 \times 10^6$, the best overall scaling is achieved with $a = -0.2229$, $b = -0.03359$ and $c = 0.04695$. Figure 3(*b*) shows the Rayleigh-number dependence using the new non-dimensionalization. The dependence has indeed decreased for most correlations, but the correlations $\overline{c_\theta a_p}/\rho$, $\overline{b_\theta b_2}$ and $\overline{(\partial b_\theta/\partial y)a_p}/\rho$ still show a significant variation with Ra.

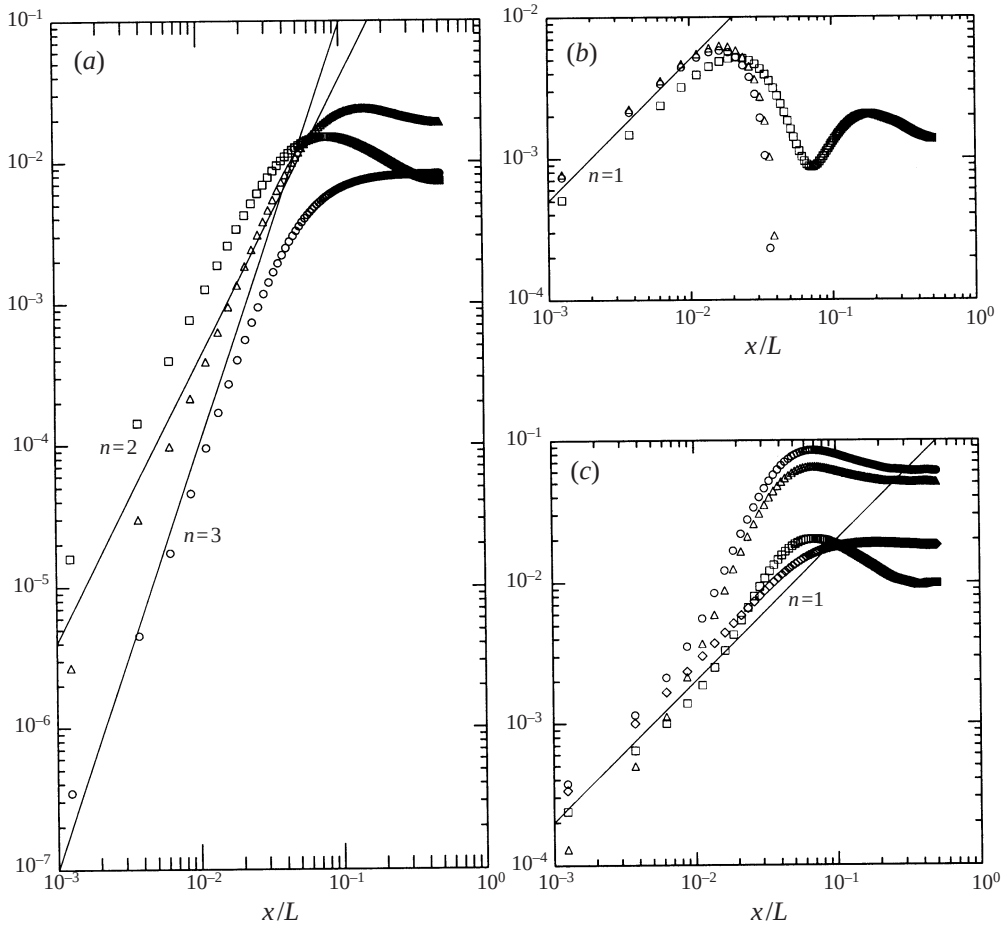

FIGURE 2. The near-wall slopes of (*a*) $\overline{\theta u_i}$ (○, $i = 1$; △, $i = 2$) and $\overline{\theta^2}$ (□), (*b*) $\mathscr{D}^v_{\theta 1}$ (○), $\hat{\mathscr{D}}^v_{\theta 1}$ (△) and $\varepsilon_{\theta 1}$ (□), (*c*) $-\mathscr{D}^p_{\theta 1} + \mathscr{D}^p_{\theta 1}|_w$ (○), $\Phi_{\theta 1} - \Phi_{\theta 1}|_w$ (△), $-\Pi_{\theta 1}$ (□) and $-\Pi_{\theta 2}$ (◇), all at $Ra = 5.4 \times 10^5$.

Rayleigh- and Reynolds-number independence is an important criterion for judging the model generality. In this study, the best we can show is that the model performs almost equally well over one decade of Rayleigh numbers (the range for which the DNS data are available). A proof of the Ra independence can be displayed only if proper scaling is applied separately for the near-wall and in the central region of the channel. Figure 4(*a*) shows the thermal-to-mechanical time-scale ratio $R = \overline{\theta^2}\varepsilon/(k\varepsilon_{\theta\theta})$ for all four Rayleigh numbers. At $x/L = 0.5$, R is approximately proportional to $Ra^{-0.11}$. This is still a reasonable assumption down to $x/L = 0.1$. However, for $x/L < 0.1$, it is clearly no longer valid. In figure 4(*b*), the turbulent Prandtl number $\sigma_T = (\overline{uv}\,\mathrm{d}T/\mathrm{d}x)/(\overline{\theta u}\,\mathrm{d}V/\mathrm{d}x)$ has been displayed. In the region $0.2 < x/L < 0.5$, σ_T is scattered around the constant value 0.9, which is a common choice in most turbulence models. Closer to the wall, the profiles at the different Rayleigh numbers depart when they approach the singularity at the velocity maximum around $x/L = 0.07$.

3.2. *Diffusion*

In contrast to the Reynolds-stress and temperature-variance transport equations, molecular diffusive transport of $\overline{\theta u_i}$ has to be modelled. A model (models are marked

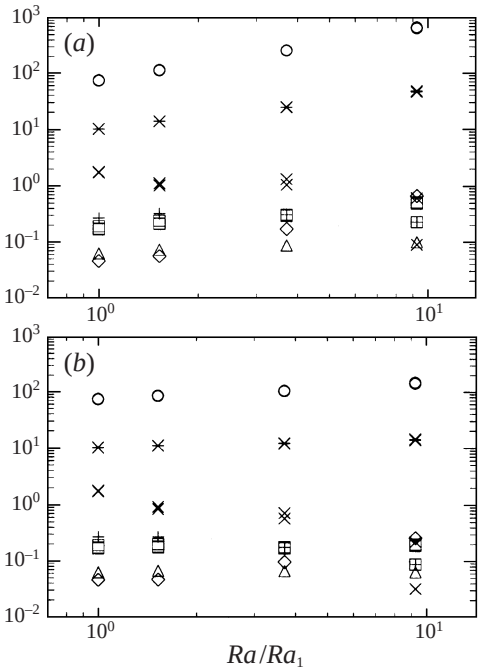

FIGURE 3. The correlations $\overline{b_\theta c_1}$ (○), $-\overline{b_\theta a_p}/\rho$ (△), $\overline{b_\theta b_p}/\rho$ (□), $-\overline{c_\theta a_p}/\rho$ (◇), $\overline{b_\theta b_2}$ (×), $-\overline{(\partial b_\theta/\partial y)a_p}/\rho$ (+) and $\overline{b_\theta^2}$ (*) at several Rayleigh numbers ($Ra_1 = 5.4 \times 10^5$) before (*a*) and after (*b*) rescaling. Multiple symbols for each correlation at a Rayleigh number correspond to various origins, from which the correlations were deduced, see table 2.

$c_\theta^{(1)}$	$c_\theta^{(2)}$	$c_{\theta\theta}^{(1)}$	$c_{\theta\theta}^{(2)}$	$c_{\theta\theta}^{(3)}$	R
0.11	0.22	0.05	0.11	0.22	0.5

TABLE 3. The coefficients appearing in the diffusion and dissipation models.

with the 'hat' symbol) that satisfies the near-wall balance and the wall values (see table 1) is given by the first line of the following equation:

$$\hat{\mathscr{D}}_{\theta i}^{\nu} = \frac{1}{2}(\alpha+\nu)\frac{\partial^2\overline{\theta u_i}}{\partial x_k^2} = \mathscr{D}_{\theta i}^{\nu} + \frac{1}{2}(\alpha-\nu)\theta\overline{\frac{\partial^2 u_i}{\partial x_k}} - \frac{1}{2}(\alpha-\nu)\overline{\frac{\partial^2\theta}{\partial x_k^2}u_i}. \tag{3.9}$$

The second line shows that viscous diffusion does not need modelling when $Pr = 1$. It can be shown, using the DNS data of Versteegh & Nieuwstadt (1998), that equation (3.9) is an excellent model for the present problem. Due to a large difference between the typical scales of the fluctuations and their second derivatives, the correlations in the last two terms of equation (3.9) are small.

The turbulent-diffusion term of the turbulent-heat-flux budget contains the triple correlation $\overline{\theta u_i u_k}$. The usual modelling strategy is to simplify the (exact) transport equation for the triple correlation to an algebraic expression in terms of known quantities (see Hanjalić & Launder (1972) for $\overline{u_i u_j u_k}$). The simplification consists

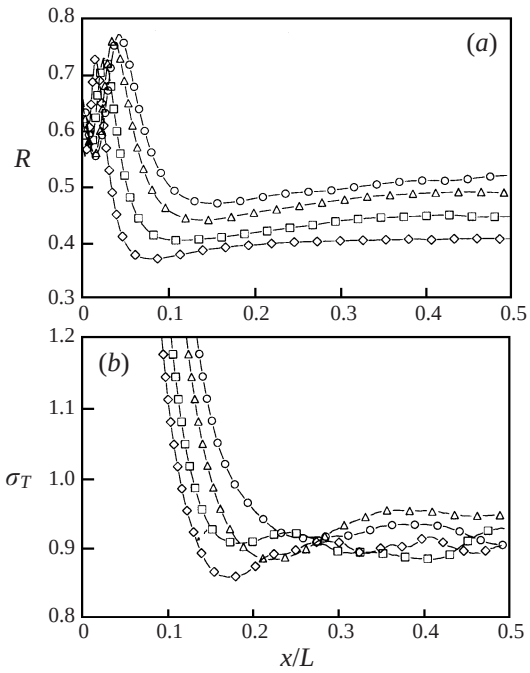

FIGURE 4. The time-scale ratio R (a) and the turbulent Prandtl number σ_T (b) at several Rayleigh numbers (–○– : $Ra = 5.4 \times 10^5$, –△– : $Ra = 8.227 \times 10^5$, –□– : $Ra = 2 \times 10^6$, –◇– : $Ra = 5 \times 10^6$).

of neglecting all terms containing the derivatives of third moments, except for the pressure term, and expressing the fourth moments in terms of second moments using the zero-fourth-cumulant hypothesis of Millionshchikov (see Monin & Yaglom 1975). By modelling the pressure term with a linear 'slow' model, the following expression is obtained:

$$\hat{\mathscr{D}}^{\mathrm{t}}_{\theta i} = \frac{\partial}{\partial x_k}\left[c_\theta \frac{k}{\varepsilon}\left(\overline{u_k u_l}\frac{\partial \overline{\theta u_i}}{\partial x_l} + \overline{u_i u_l}\frac{\partial \overline{\theta u_k}}{\partial x_l} + \overline{\theta u_l}\frac{\partial \overline{u_i u_k}}{\partial x_l}\right)\right] \tag{3.10}$$

with usually $c_\theta = 0.11$ ($c_\theta^{(1)}$, see table 3). The last term of equation (3.10), which has a character of an additional source in the equation for $\overline{\theta u_i}$, is often omitted, providing a simpler expression which consists of heat-flux gradients only and which is still invariant under coordinate rotation. Dol, Hanjalić & Kenjereš (1997) showed that this simplification is useful and appropriate for the present vertical channel. If the second term is also omitted, the well-known gradient-diffusion hypothesis of Daly & Harlow (1970) is obtained. That model, which is not invariant and is inferior to the former one (see Dol *et al.* 1997), needs a larger coefficient, such as 0.22 ($c_\theta^{(2)}$, see table 3).

A model for turbulent diffusion of the temperature variance can be derived in the same way. In this case, however, the production of the triple correlation $\overline{\theta^2 u_k}$ needs to be included for acceptable performance (Dol *et al.* 1997). The invariant model expression is

$$\hat{\mathscr{D}}^{\mathrm{t}}_{\theta\theta} = \frac{\partial}{\partial x_k}\left[c_{\theta\theta}\frac{k}{\varepsilon}\left(\overline{u_k u_l}\frac{\partial \overline{\theta^2}}{\partial x_l} + 2\overline{\theta u_l}\frac{\partial \overline{\theta u_k}}{\partial x_l} + 2\widehat{\overline{\theta u_k} u_l}\frac{\partial T}{\partial x_l}\right)\right], \tag{3.11}$$

$$\widehat{\overline{\theta u_i u_k}} = -c_\theta^{(2)} \frac{k}{\varepsilon} \left(\overline{u_k u_l} \frac{\partial \overline{\theta u_i}}{\partial x_l} + \overline{u_i u_l} \frac{\partial \overline{\theta u_k}}{\partial x_l} \right). \tag{3.12}$$

Only thermal production is included, because this is the only non-zero production budget term of $\overline{\theta^2 u}$. The full expression needs $c_{\theta\theta} = 0.05$ ($c_{\theta\theta}^{(1)}$, table 3). Omitting the last term of equation (3.11) leads to the usual invariant model with $c_{\theta\theta} = 0.11$ ($c_{\theta\theta}^{(2)}$, table 3). The Daly & Harlow model, with $c_{\theta\theta} = 0.22$ ($c_{\theta\theta}^{(3)}$, table 3), is obtained when only the first term is retained.

3.3. *Dissipation*

The dissipation rate of the turbulent heat flux is usually neglected. Although this is justified only when the turbulence is isotropic, at least at the smallest scales, in the flow considered here the DNS show that this is indeed a relatively small budget term, even near the walls where the largest and smallest scales are comparable. Unlike for the Reynolds stress, the dissipation does not balance the production. Instead, the production of $\overline{\theta u_i}$ is balanced mainly by the (total) pressure scrambling, which is a negative budget term throughout the channel. The dissipation of $\overline{\theta u_i}$ merely balances viscous diffusion in the near-wall region. The following dissipation model satisfies the above condition near a solid wall:

$$-\hat{\varepsilon}_{\theta i} = -f^* \varepsilon_{\theta i}^* - \varepsilon_{\theta i}', \tag{3.13}$$

$$-\varepsilon_{\theta i}^* = -\frac{1}{2} \left(1 + \frac{1}{Pr} \right) \frac{\varepsilon}{k} \overline{\theta u_i}, \tag{3.14}$$

$$-\varepsilon_{\theta i}' = -\frac{1}{2} \hat{\mathscr{D}}_{\theta i}^{\nu} + \frac{1}{4} \left(1 + \frac{1}{Pr} \right) \frac{\mathscr{D}_k^{\nu}}{k} \overline{\theta u_i}, \tag{3.15}$$

$$f^* = \exp\left(-\tfrac{3}{4} A^{3/2}\right), \tag{3.16}$$

where A is a stress invariant (see the next subsection). This model is obtained following Hanjalić, Jakirlić & Ristorcelli (1997*b*) for the dissipation of the Reynolds-stress tensor. A slight disadvantage of the model is that it contains the second derivative of $k = \overline{u_i^2}/2$ ($\mathscr{D}_k^{\nu} = \nu \partial^2 k / \partial x_k^2$), which necessitates a fine grid for accurate solutions. However, unlike other published models, which apply topology-dependent parameters such as wall normals or distances (e.g. Peeters & Henkes 1992), the model proposed here satisfies wall constraints using only local flow properties. In figure 5, equation (3.13) is evaluated by feeding the DNS results for variables on the right-hand side of equations (3.13)–(3.16) and compared with the DNS data for $\varepsilon_{\theta i}$. The figure shows that the new dissipation model performs equally well at all available Rayleigh numbers. Note that the scale in figure 5(*a*) is much finer than in figure 5(*b*) because $\varepsilon_{\theta 1} \ll \varepsilon_{\theta 2}$, so that a failure to reproduce the second peak in $\varepsilon_{\theta 1}$ in the near-wall region is not a serious deficiency of the model as a whole.

In the transport equation for the temperature variance, beside turbulent diffusion, only the dissipation needs modelling. Contrary to a common belief, the dissipation rate $\varepsilon_{\theta\theta}$ is not the weak spot of the closure. For a vertical channel, it appears to be sufficient to assume a constant thermal-to-mechanical time-scale ratio R. The model then becomes $\hat{\varepsilon}_{\theta\theta} = \varepsilon \overline{\theta^2} / (Rk)$. From figure 4(*a*), it follows that $R = 0.5$ is a good choice for $0.1 < x/L < 0.5$ at $Ra = 5.4 \times 10^5$. Close to a wall for $x/L < 0.1$, R varies substantially exhibiting a peak around $x/L \approx 0.05$, but this behaviour has a much smaller effect on $\hat{\varepsilon}_{\theta\theta}$ than expected. In § 4, it will be demonstrated that, together with the full model for turbulent diffusion (i.e. all terms of equation (3.11)),

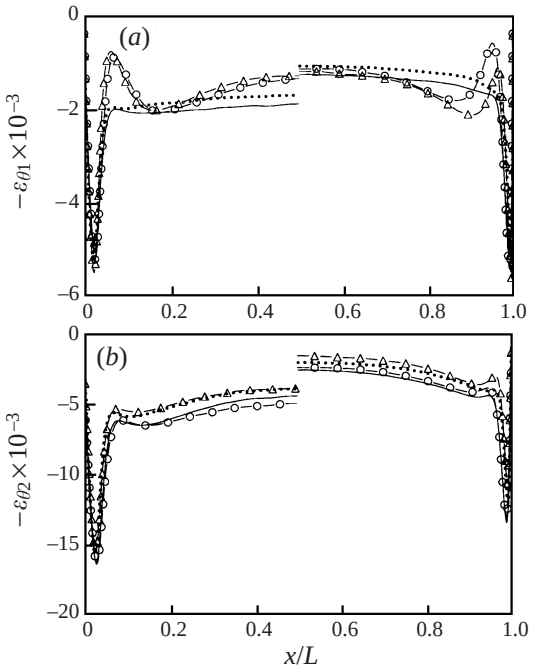

FIGURE 5. Performance of the new dissipation model at several Rayleigh numbers. For $x/L < 0.5$: model (—, $Ra = 5.4 \times 10^5$; ···, $Ra = 8.227 \times 10^5$) evaluated/compared with DNS (–◯–, $Ra = 5.4 \times 10^5$; –△–, $Ra = 8.227 \times 10^5$). For $x/L > 0.5$: model (—, $Ra = 2 \times 10^6$; ···, $Ra = 5 \times 10^6$) evaluated/compared with DNS (–◯– : $Ra = 2 \times 10^6$, –△– : $Ra = 5 \times 10^6$).

$R = 0.5$ closes the equation very well, though for $Ra = 5 \times 10^6$ $R = 0.4$ would have been a better choice. This Rayleigh-number dependence, considered earlier, is actually a larger problem than the x/L dependence. A possible solution is to adopt $R = \min(2.2Ra_t^{-0.13}, 0.75)$, which follows the DNS value for R at $x/L = 0.5$ accurately and which is almost constant for $0.1 < x/L < 0.5$ in the considered range of Rayleigh numbers. In this expression, $Ra_t = g\beta(\overline{\theta^2})^{1/2}k^{9/2}Pr/(\nu^2\varepsilon^3)$ is the turbulence Rayleigh number, which is a local property.

3.4. *Pressure scrambling*

The remaining budget term in the turbulent-heat-flux equation (3.1) that needs (re)modelling is the pressure scrambling $\Pi_{\theta i}$. Figure 6 shows that, of the unclosed budget terms, the pressure scrambling is the most dominant one. Consequently, accurate modelling of this term is crucial for the performance of the complete model. Because pressure fluctuations are impossible to measure accurately, modelling and validation of the correlations involving pressure depends completely on the availability of DNS data.

The total pressure term $\Pi_{\theta i}$ can be written as the sum of $\Phi_{\theta i} = \overline{(\partial\theta/\partial x_i)p}/\rho$ and $\mathscr{D}^p_{\theta i} = -(\partial\overline{\theta p}/\partial x_i)/\rho$. This splitting was originally introduced for the corresponding term in the Reynolds-stress budget, because the pressure–strain term is redistributive (i.e. tensor has zero trace) and the remaining pressure transport has a divergence character. Although not unique (Lumley 1975), compared with other proposals this splitting seems physically most justified and the only one which satisfies the two-component limit and the condition of zero pressure transport in the homogeneous (e.g. spanwise) direction in two-dimensional flows (Groth 1991). However, none of

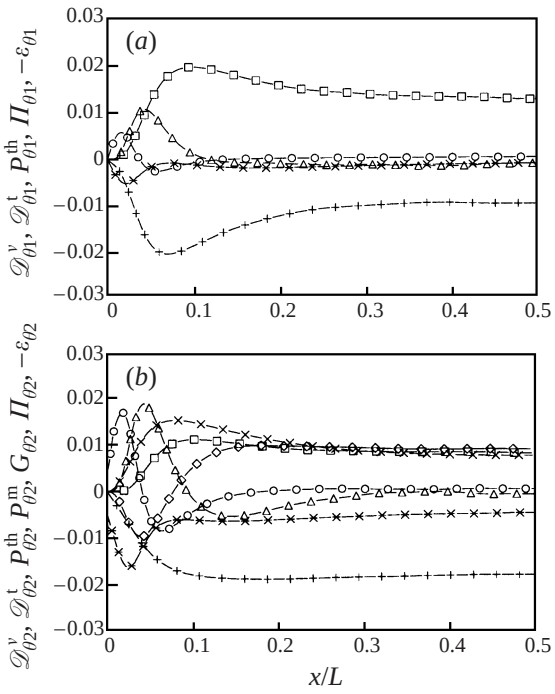

FIGURE 6. The DNS budget terms of $\overline{\theta u_i}$ at $Ra = 5.4 \times 10^5$ for $i = 1$ (*a*) and $i = 2$ (*b*): viscous (–◯–) and turbulent (–△–) diffusion, thermal (–□–), mechanical (–◇–) and buoyant (–×–) production, pressure scrambling (–+–) and dissipation (–*–).

the splittings proposed in the literature seems justified when dealing with a vector quantity. Besides, the separate terms appear to be much more difficult to model than the total pressure term. This is particularly true close to the wall where they exhibit steep, though opposing, variations. This is also true for the pressure scrambling term in the stress equation, and despite a clearer physical identification of the terms, modelling the total term may prove to be more satisfactory. Dol *et al.* (1997) showed that the pressure diffusion is substantial in the near-wall region, so that the standard practice of neglecting this term is obviously incorrect. All these facts are in favour of modelling $\Pi_{\theta i}$ as a whole and, by following this route, we do not consider pressure diffusion any further.

Irrespective of whether the pressure scrambling term will be modelled in its original or transformed form (i.e. without or with splitting), for further discussion of the adopted modelling approach it is useful to recall the Poisson equation for the correlation between the pressure fluctuations and any other fluctuating property ϕ (here θ or $\partial\theta/\partial x_i$) at a location x_i inside the volume $\mathscr{V}$ bounded by the surface $\mathscr{S}$:

$$\frac{\overline{\phi p}}{\rho} = \frac{1}{4\pi}\int_{\mathscr{V}} \left[\overline{\phi \left(\frac{\partial^2 u_k u_l}{\partial x_k \partial x_l}\right)'} + 2\overline{\phi \left(\frac{\partial u_l}{\partial x_k}\right)'\left(\frac{\partial U_k}{\partial x_l}\right)'} + g_k \beta \overline{\phi \left(\frac{\partial \theta}{\partial x_k}\right)'} \right] \frac{\mathrm{d}\mathscr{V}}{r}$$

$$+ \frac{1}{4\pi}\oint_{\mathscr{S}} \left[\frac{1}{r}\overline{\frac{\phi}{\rho}\left(\frac{\partial p}{\partial n}\right)'} - \frac{\overline{\phi p'}}{\rho}\frac{\partial (1/r)}{\partial n} \right] \mathrm{d}\mathscr{S} \qquad (3.17)$$

where $\partial/\partial n$ is the outward normal derivative and $r = \|x_i' - x_i\|$ (x_i' is the running

coordinate). The surface integral (Stokes, harmonic term) is expected to play an important role in the near-wall flows (small r). The equation contains two-point correlations and is of little direct use. However, the physical meaning of each of the four terms can be identified. The linear character of the Poisson equation enables separate DNS of each contributing term, as well as their separate modelling. We, therefore, adopt the conventional route of expressing the pressure scrambling term as a sum of four contributions corresponding to each term in the Poisson equation:

$$\Pi_{\theta i} = \Pi_{\theta i,1} + \Pi_{\theta i,2} + \Pi_{\theta i,3} + \Pi_{\theta i}^{\mathrm{w}}. \tag{3.18}$$

Here $\Pi_{\theta i,1}$ represents pure turbulence interactions (the 'return-to-isotropy' or 'slow' term), $\Pi_{\theta i,2}$ is the 'rapid' part involving the effect of mean strain, $\Pi_{\theta i,3}$ is the buoyancy contribution and $\Pi_{\theta i}^{\mathrm{w}}$ is the wall-reflection (Stokes) term.

Decomposing the pressure correlation according to the terms in the Poisson equation simplifies modelling, as it presets an assumed conceptual framework confining the attention only to the quantities appearing explicitly in this equation. It is noted that the Poisson equation does not include directly the mean temperature gradient. However, physical reasoning suggests that the mean temperature gradient undoubtedly affects the pressure scrambling process.† We, therefore, separately model each term in equation (3.18), but merge the rapid and buoyant parts, which are in fact both 'rapid' (see Lumley 1978, p. 144), enhanced with the mean-temperature gradient.

Figure 7 shows the terms in $\Pi_{\theta i}$ (equation (3.18)) provided by the DNS database at $Ra = 5.4 \times 10^5$. Versteegh & Nieuwstadt (1998) did not explicitly evaluate terms in equation (3.17), but solved separately the Poisson equation for each part applying homogeneous Neumann boundary conditions. The wall part follows from the Laplace equation with the boundary conditions for the pressure fluctuation supplied by the database. The figure shows that the slow part dominates the pressure scrambling and that the wall part is relatively small.

3.4.1. *Model of the slow term*

In the absence of any turbulence production and source of anisotropy, the turbulence interaction part $\Pi_{\theta i,1}$ is expected to isotropize the turbulent flux $\overline{\theta u_i}$. The rate of isotropization will depend on the initial degree of anisotropy of both the fluctuating temperature and velocity fields, which can be represented by $\overline{\theta u_i}$, $a_{ij}^{\theta} = \overline{\theta u_i}\,\overline{\theta u_j}/\overline{\theta u_k}^2 - \delta_{ij}/3$ and $a_{ij} = \overline{u_i u_j}/k - 2\delta_{ij}/3$. In order to keep the model relatively simple, we expand the expression with a quadratic and a cubic term. The expression is still linear in $\overline{\theta u_i}$ and up to quadratic in a_{ij} (the latter to comply with the quadratic model for the slow term in the stress equation), which is the complete form of its tensorial expansion (Speziale, Sarkar & Gatski 1991):

$$\hat{\Pi}_{\theta i,1} = -\frac{\varepsilon}{k}(c_{1\theta}\overline{\theta u_i} + c'_{1\theta} a_{ij}\overline{\theta u_j} + c''_{1\theta} a_{ij} a_{jk}\overline{\theta u_k}). \tag{3.19}$$

The coefficients are given in table 4. For $c'_{1\theta} = c''_{1\theta} = 0$ and $c_{1\theta}$ constant, the model reduces to the linear slow part of the basic model. The designation 'basic model' is generally used for the high-Re_{t} second-moment closure of the 1970s, which is characterized by the use of linear pressure-correlation models with wall-topology parameters introduced to account for the wall-blockage effects (for a review, see

† Jones & Musonge (1983) proposed a lump model of both the slow and rapid terms for forced scalar transport (no buoyancy), in which they included the mean temperature gradient, arguing that both the mean velocity and mean temperature gradients appear in the exact equation for the slow part, derived from the transport equation for the two-point correlation.

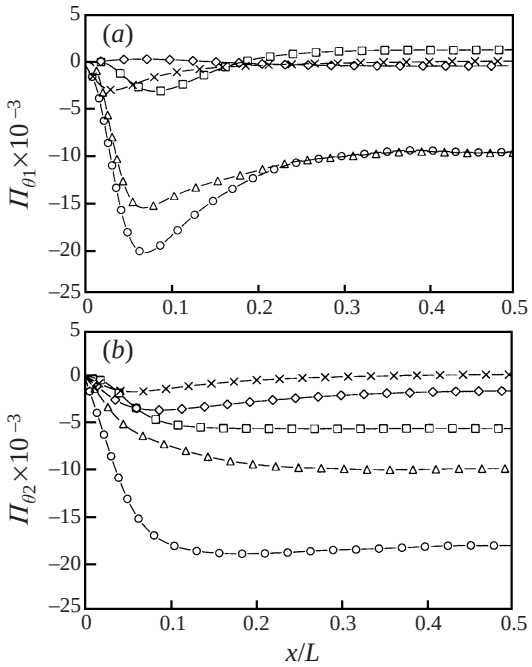

FIGURE 7. Decomposition of $\Pi_{\theta i}$ at $Ra = 5.4 \times 10^5$ for $i = 1$ (*a*) and $i = 2$ (*b*): total (–◯–), slow (–△–), rapid (–□–), buoyant (–◇–) and wall part (–×–).

$c_{1\theta}$	$c_{2\theta}$	$c_{3\theta}^{(1)}$	$c_{3\theta}^{(2)}$	$c_{1\theta}^{\mathrm{w}}$	c_{w}
3.75	0.5	0.5	0.45	0.2	2.53

TABLE 4. The coefficients of the pressure-scrambling models. All of them, except for $c_{3\theta}^{(2)}$, are used in the basic model.

Launder 1989). For forced convection, Launder proposed $c_{1\theta} = 3.0$ (Gibson & Launder 1978), which was also found by Hanjalić & Vasić (1993) to be a reasonable value for buoyant flow, whereas Peeters & Henkes (1992) adopted $c_{1\theta} = 3.75$ for the natural-convection boundary layer. Note the similarity between the basic slow model and the dissipation model (3.14). However, figure 8 shows the linear model for $c_{1\theta} = 1$, evaluated from the DNS data at $Ra = 5.4 \times 10^5$, indicating clearly that the linear model is inadequate: no value nor (scalar) function for $c_{1\theta}$ will be able to match the DNS data for both components. This was the reason for introducing higher-order terms in the present work.

The quadratic and cubic terms in equation (3.19) are depicted in figure 8, with $c'_{1\theta} = c''_{1\theta} = 1$. Referring to Jones & Musonge (1983), Craft & Launder (1989) add a fourth term, proportional to $-ka_{ij}\partial T/\partial x_j$ to equation (3.19), which they found helpful in reproducing the experiment of Tavoularis & Corrsin (1985). The influence on the predictions of the other flows tested is said to be small.

If the coefficients are kept constant, even with the inclusion of quadratic and cubic terms, equation (3.19) cannot reproduce the DNS of $\Pi_{\theta i,1}$, particularly close to the wall. This can be demonstrated by solving equation (3.19) for three components using

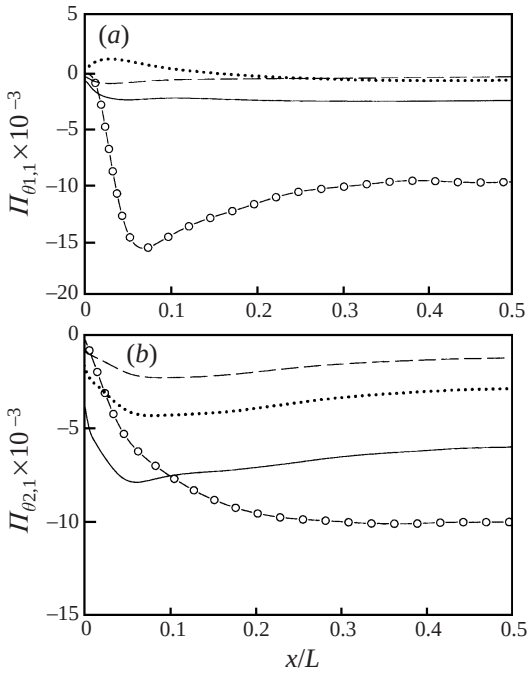

FIGURE 8. The slow part $\Pi_{\theta i,1}$ (–◯–) at $Ra = 5.4 \times 10^5$ for $i = 1$ (a) and $i = 2$ (b) compared with the variation of each, the linear (—), quadratic (· · ·) and cubic (– –), terms in equation (3.19) for $c_{1\theta} = c'_{1\theta} = c''_{1\theta} = 1$.

the DNS data to find the variation of coefficients $c_{1\theta}$, $c'_{1\theta}$ and $c''_{1\theta}$. In the flow considered here only two components of the heat flux are non-zero and either a model with two terms needs to be considered, or an additional constraint needs to be introduced. Both options are discussed below, together with possible modelling of the coefficients in terms of local invariant turbulence parameters. For this purpose we considered invariants of the stress tensor, $A_2 = a_{ij}a_{ji}$, $A_3 = a_{ij}a_{jk}a_{ki}$ and $A = 1 - 9(A_2 - A_3)/8$. Figure 9(a) shows the variation of all three invariants as a function of x/L. It should be recalled that $A = 0$ for two-component turbulence, such as found close to the walls where $\overline{u^2}$ is much smaller than $\overline{v^2}$ and $\overline{w^2}$, and $A = 1$ for an isotropic stress field. In the centre of the vertical channel $A \approx 0.66$ indicating that the flow is not completely isotropic. However, the fact that A is a local property that varies monotonically between its extreme values with the strongest variation in the near-wall region, makes it a very useful parameter. Besides, multiplying a model with A^n ($n > 0$) ensures that the two-component limit is satisfied.

Figure 9(b) shows the well-known invariant map, introduced by Lumley & Newman (1977). All realizable states of turbulence are within the triangle, with the limiting states on its boundaries: three-component isotropy ($A = 1$) at $(0, 0)$, two-component isotropy at $(-2/9, 2/3)$ and one-component turbulence at $(16/9, 8/3)$. Anisotropic two-component turbulence is marked by the straight line ($A = 0$), while the curved lines ($A_2 = 6(|A_3|/6)^{2/3}$) indicate the axisymmetric states of turbulence (axial component smaller for $A_3 < 0$, larger for $A_3 > 0$). We see that both close to the walls and in the centre the turbulence is almost axisymmetric. In this study, we only use mechanical invariants. Our reasons for this decision are: (i) the Prandtl number is close to unity; (ii) only the mechanical time scale k/ε is used (allowed as R

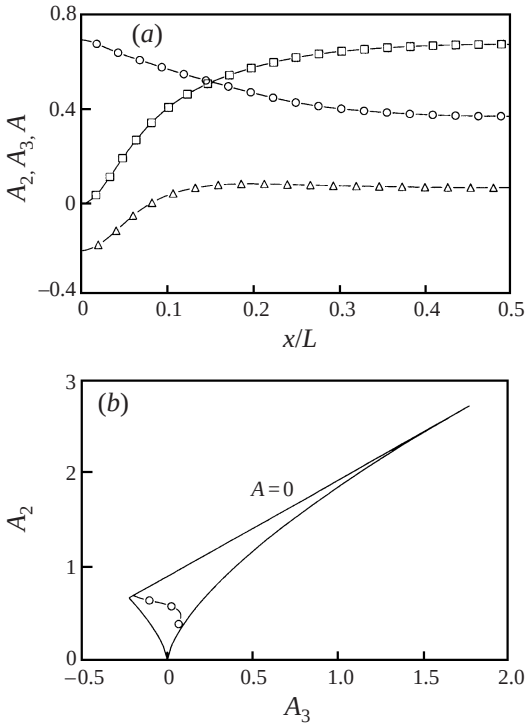

FIGURE 9. (*a*) The stress invariants A_2 (–○–), A_3 (–△–) and A (–□–) as a function of the distance to the wall. (*b*) The A_2, A_3 characteristic (–○–) enclosed by the Lumley triangle of realisable turbulence states.

is approximately constant); (iii) a thermal analogy to the Lumley triangle does not exist. Some thermal invariants have been proposed, such as the normalized correlation function $(\overline{\theta u_k})^2/(\overline{\theta^2}\,\overline{u_l^2})$ or the more complicated mixed tensor of Shih, Lumley & Chen (1988), but their interpretation is less straightforward and their use did not improve our results.

When only two terms are retained in equation (3.19), a system of two equations (for $i = 1$ and $i = 2$) with two unknowns ($c_{1\theta}$ and $c'_{1\theta}$) results. The solution of the system is displayed in figure 10(*a*) as a function of A. The figure shows that $c_{1\theta}$ is positive, $c'_{1\theta}$ negative and $-c'_{1\theta}/c_{1\theta} \approx 1.4$, which supports choices made in the literature. The shapes of $c_{1\theta}$ and $c'_{1\theta}$ can be approximated by functions of the following type:

$$c_{1\theta}, c'_{1\theta}, c''_{1\theta} \subset F_{pqrs}(A) = \frac{p[1 - \exp(-qA)]}{1 + r\exp(-sA)}. \tag{3.20}$$

The parameters r and s are mainly used for fine-tuning in the near-wall region. The optimum set of shape parameters is given by table 5, 'model 1'. The performance of the resulting model is depicted in figure 10(*b*). A disadvantage of the model is its sensitivity to the functions (3.20). For example, when only one function is used together with $-c'_{1\theta}/c_{1\theta} = 1.4$, $\Pi_{\theta i,1}$ exhibits substantial oscillations in the near-wall region. The oscillations can only be suppressed by using two functions that are tuned very accurately. This sensitivity decreases when the third term is added to the model. The resulting system can only be solved when an additional 'equation' is posed. At

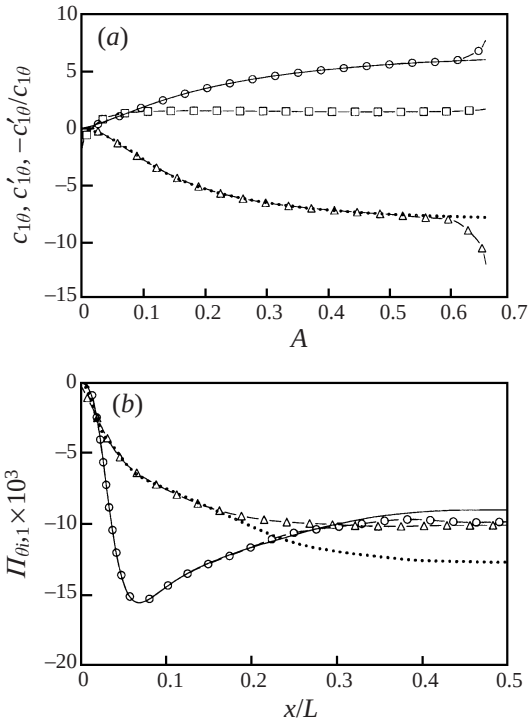

FIGURE 10. (*a*) The 'exact' profiles for $c_{1\theta}$ (–○–), $c'_{1\theta}$ (–△–), their approximations (—, ···) and the ratio $-c'_{1\theta}/c_{1\theta}$ (–□–) when $c''_{1\theta} = 0$. (*b*) The performance of the resulting slow model for $i = 1$ (—; –○–, DNS) and $i = 2$ (···; –△–, DNS). All graphs are at $Ra = 5.4 \times 10^5$.

	model 1			model 2		
	$c_{1\theta}$	$c'_{1\theta}$	$c''_{1\theta}$	$c_{1\theta}$	$c'_{1\theta}$	$c''_{1\theta}$
p	6.4	−8.1	0	4.9	$-2c_{1\theta}$	12.9
q	4.0	5.5		3.6	∞	1.2
r	1.0	4.5		10	0	−0.94
s	20	28		37		10

TABLE 5. The values for the shape factors constituting $F_{pqrs}(A)$ for the two new slow-part models, optimized at $Ra = 5.4 \times 10^5$.

first, $-c'_{1\theta}/c_{1\theta} = 1.4$ seemed to be a natural choice. The corresponding solution for $c_{1\theta}$ and $c''_{1\theta}$ is displayed in figure 11(*a*). Obviously, the shapes will be very hard to match. However, using $-c'_{1\theta}/c_{1\theta} = 2$ produced more convenient shapes, which were easier to model, as shown in the same figure. The values of the shape parameters for this case are also given in table 5, 'model 2'. The shape of $c''_{1\theta}$ is more sensitive to the ratio than $c_{1\theta}$. Both slow models are less satisfactory in the central channel region due to the 'tails' in the profiles for $c_{1\theta}$ and c'_{θ} at $A > 0.6$, corresponding to $0.25 < x/L < 0.5$. Because of the absence of such a tail in the profile for $c''_{1\theta}$, the second model is somewhat more accurate in the central region, although a deviation remains in the other component. The non-physical 'tails' point out a deficiency of equation (3.19), but fortunately this deviation is confined to the centre of the duct

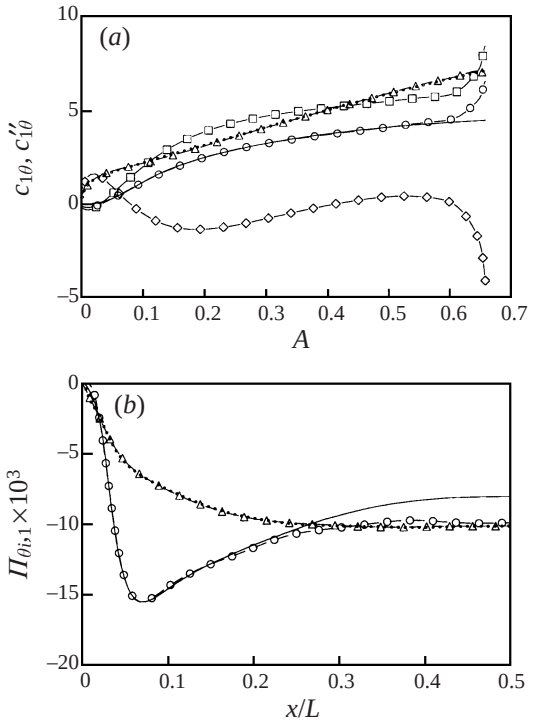

FIGURE 11. (*a*) The 'exact' profiles for $c_{1\theta}$ (–□–) and $c''_{1\theta}$ (–◇–) when $-c'_{1\theta}/c_{1\theta} = 1.4$ and for $c_{1\theta}$ (–○–), $c''_{1\theta}$ (–△–) and their approximations (—, ···) when $-c'_{1\theta}/c_{1\theta} = 2$. (*b*) The performance of the resulting slow model for $i = 1$ (—; –○–, DNS) and $i = 2$ (···; –△–, DNS). All graphs are at $Ra = 5.4 \times 10^5$.

and has no effect on the model performance in the rest of the flow. In figure 12, the performance of the slow-part models is depicted for all four Rayleigh numbers. Surprisingly, the quadratic model is somewhat better for the highest two Rayleigh numbers.

3.4.2. *Model of the rapid and buoyant terms*

$\Pi_{\theta i,2}$ and $\Pi_{\theta i,3}$ are interpreted as the action of pressure fluctuations to isotropize the process of turbulence production due to mean strain rate and buoyancy, respectively. In the absence of an exact foundation, the models of rapid and buoyant terms are usually derived on the basis of representation theory (e.g. Lumley 1975). The mean strain rate is taken outside the integral, assuming homogeneity or that the two-point correlations are only significant for small r over which the mean flow does not change appreciably. The remainder of the integral (higher rank tensor) is expressed in the form of a tensorial expansion in terms of irreducible vectors and tensors (integrity basis), formed from the quantities which appear in the integral. A number of the coefficients are then deduced using symmetry and kinematic constraints. In the present case this approach would lead to

$$\Pi_{\theta i,2/3} = \Pi_{\theta i,2} + \Pi_{\theta i,3} = F_i\left(\overline{\theta u_i}, g_i, \frac{\partial T}{\partial x_i}, a_{ij}, S_{ij}, \Omega_{ij}\right) \tag{3.21}$$

where $S_{ij} = \frac{1}{2}(\partial U_i/\partial x_j + \partial U_j/\partial x_i)$ and $\Omega_{ij} = \frac{1}{2}(\partial U_i/\partial x_j - \partial U_j/\partial x_i)$.

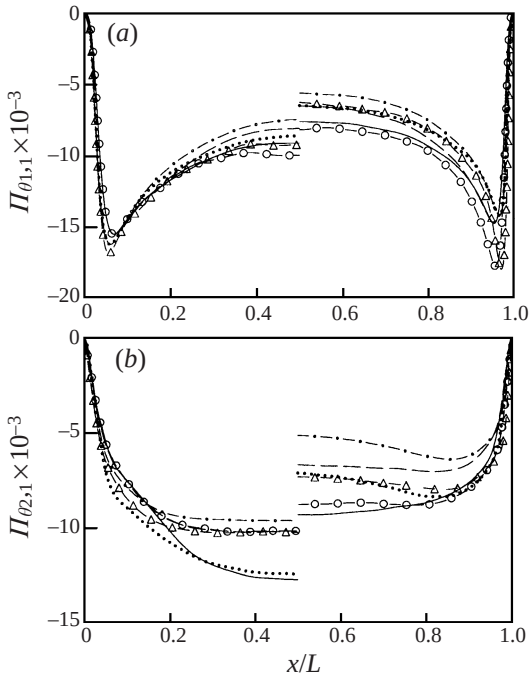

FIGURE 12. The performance of the new slow models at several Rayleigh numbers. For $x/L < 0.5$: quadratic (—, $Ra = 5.4 \times 10^5$; ···, $Ra = 8.227 \times 10^5$) and cubic (– –, $Ra = 5.4 \times 10^5$; –·–, $Ra = 8.227 \times 10^5$) models evaluated/compared with DNS (–◯–, $Ra = 5.4 \times 10^5$; –△–, $Ra = 8.227 \times 10^5$). For $x/L > 0.5$: quadratic (— , $Ra = 2 \times 10^6$; ···, $Ra = 5 \times 10^6$) and cubic (– –, $Ra = 2 \times 10^6$; –·–, $Ra = 5 \times 10^6$) models evaluated/compared with DNS (–◯–, $Ra = 2 \times 10^6$; –△–, $Ra = 5 \times 10^6$).

Craft & Launder (1989) derived their rapid model from a general expression, linear in the mean strain and turbulent heat flux and up to quadratic in a_{ij} (consistent with their slow model), the parameters of which are determined by several kinematic constraints and computer optimization for homogeneous shear flows and plane/round jets. The resulting expression outweighs in complexity all other terms in the transport equation for $\overline{\theta u_i}$ and contains a number of additional coefficients to be determined. An analogous approach for the pressure–strain term in the stress equation, closed with the Caley–Hamilton theorem, which satisfies the realizability conditions, requires terms up to cubic in a_{ij}.

It should be recalled that the representation theorem and general tensorial expansion are purely kinematic and their success in representing a physical process depends on the proper choice and availability of the irreducible vectors and tensors which, in turn, depend on the model adopted as a whole. Nonlinear models may have multiple roots which can lead to non-unique solutions even for a uniquely defined steady flow. Speziale *et al.* (1991) pointed out that models which are nonlinear in a_{ij} are inconsistent with the fact that the rapid part of the Poisson equation for the pressure–strain correlation is linear in the energy spectrum. They also showed that the general nonlinear tensorial expansion for the pressure-scrambling term in the stress equation reduces exactly to the linear form for homogeneous two-dimensional flow. More urgent than nonlinear expansion is the need to relax the mean-flow homogeneity assumption, particularly for the near-wall region, as discussed by Launder & Tselepidakis (1991).

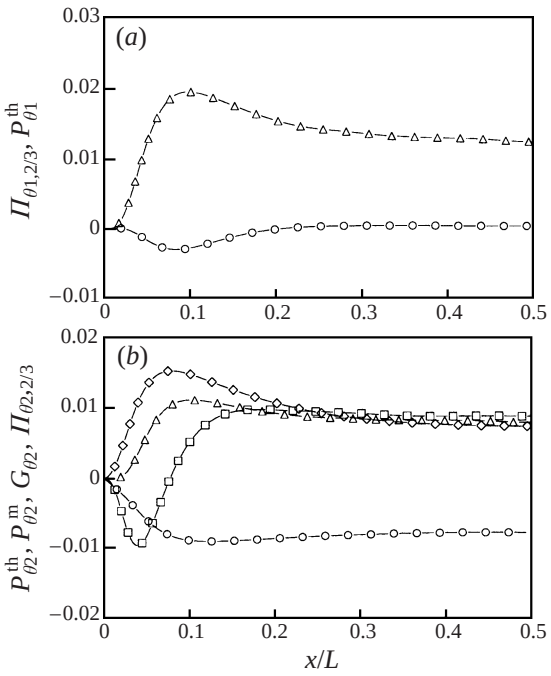

FIGURE 13. The rapid/buoyant part $\Pi_{\theta i,2/3}$ (–○–) from DNS at $Ra = 5.4 \times 10^5$ for $i = 1$ (a) and $i = 2$ (b) compared with the thermal (–△–), mechanical (–□–) and buoyant (–◇–) production.

In view of the above discussion we adopt here the simple expansion of equation (3.21) for the sum of rapid and buoyant terms, which is linear in second moments $\overline{\theta u_i}$ and $\overline{u_i u_j}$, and includes the mean temperature gradient. The expression can conveniently be written in terms of production rates:

$$\hat{\Pi}_{\theta i,2/3} = -c_{2\theta} P^{\rm m}_{\theta i} - c'_{2\theta} P^{\rm th}_{\theta i} - c_{3\theta} G_{\theta i}. \tag{3.22}$$

Of course, in order to satisfy the basic realizability constraints, coefficients cannot be constants but are functions of local invariant turbulence properties. It is recalled that the basic model does not contain the thermal production ($c'_{2\theta} = 0$) and that the remaining two coefficients are treated as constants. Peeters & Henkes (1992) take $c_{2\theta} = c_{3\theta} = 0.5$ ($c^{(1)}_{3\theta}$). The weakness of the basic model is that it yields a zero combined rapid/buoyant term $\Pi_{\theta i,2/3}$ for the horizontal component, contrary to the DNS, as shown in figure 13 for $Ra = 5.4 \times 10^5$.

The only non-zero production of the horizontal heat flux is the thermal production $P^{\rm th}_{\theta i}$. This fact provides yet another justification for including the mean temperature gradient in the rapid/buoyant model. The model function for $c'_{2\theta}$ has been tuned to match $-\hat{\Pi}_{\theta 1,2/3}/P^{\rm th}_{\theta 1}$ as closely as possible. A polynomial expression in terms of A appeared to be most suitable. The resulting function,

$$c'_{2\theta} = 6.15A^2 - 19.3A^3 + 15.0A^4, \tag{3.23}$$

is most influential in the region $0.1 < x/L < 0.5$. Figure 14(a) shows that the selected function brings the model into good agreement with the DNS.

The buoyant-production budget term multiplied by the constant value $c_{3\theta} = 0.45$ ($c^{(2)}_{3\theta}$) matches the DNS data at $Ra = 5.4 \times 10^5$ in the region $x/L < 0.05$ already quite well (see figure 14b). A function for $c_{2\theta}$ that approximates $-(\hat{\Pi}_{\theta 2,2/3} + c'_{2\theta} P^{\rm th}_{\theta 2} +$

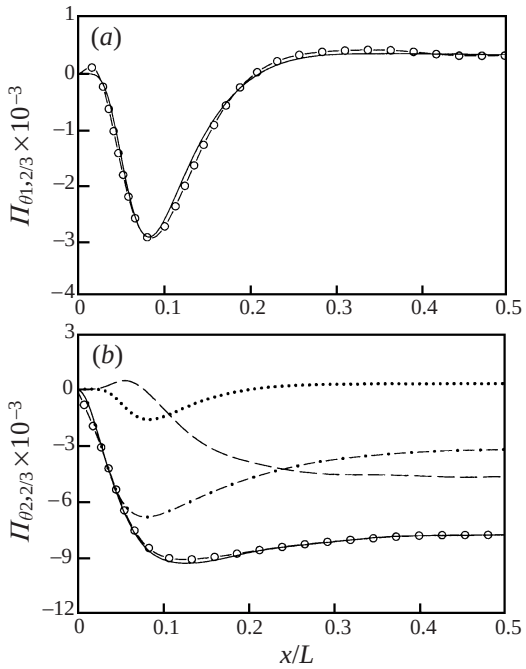

FIGURE 14. The performance of the new rapid/buoyant model (—; –◯–, DNS) at $Ra = 5.4 \times 10^5$ for $i = 1$ (*a*) and $i = 2$ (*b*). In (*b*), the thermal (· · ·), mechanical (– –) and buoyant (–·–) contributions are also distinguished.

$c_{3\theta} G_{\theta 2})/P^{\mathrm{m}}_{\theta 2}$ well, is

$$c_{2\theta} = 1.25A^2. \tag{3.24}$$

Figure 14 shows the resulting rapid/buoyant model, which is close to the DNS data throughout the channel. Figure 15 shows that the performance of the new rapid/buoyant model at the higher Rayleigh numbers is somewhat less satisfactory for the horizontal component.

3.4.3. *Model of the wall effect*

Equation (3.17) reveals two important properties of the pressure-reflection term. First, the pressure fluctuation appears inside the integral, which means that the wall term is recursive and thus proportional to the complete integral expression. Second, the wall-normal gradient introduces a preference for the horizontal component of $\Pi^{\mathrm{w}}_{\theta i}$, as seen in figure 16. Very close to the wall $\partial p/\partial n \propto \nu \partial^2 u_{\mathrm{n}}/\partial x_j^2$ indicating a viscous origin of this contribution, which is insignificant, but outside the viscous sublayer its effect is not clear. Next, there is the wall-echo effect, a name that originates from the concept of the reflected mirror image of the volume integral. The wall term permeates further from the wall, attenuating with the wall distance. Although the Stokes term as a whole is directly dependent on the wall orientation and its distance, the topology parameters are inconvenient for modelling flows with complex boundaries and need to be replaced by flow and turbulence quantities which will reflect appropriately (albeit indirectly) the wall configuration and its proximity. Of all available parameters, the stress anisotropy tensor and its invariants seem physically most appropriate, since the stress anisotropy is directly affected by the wall presence. Fortunately, the total term

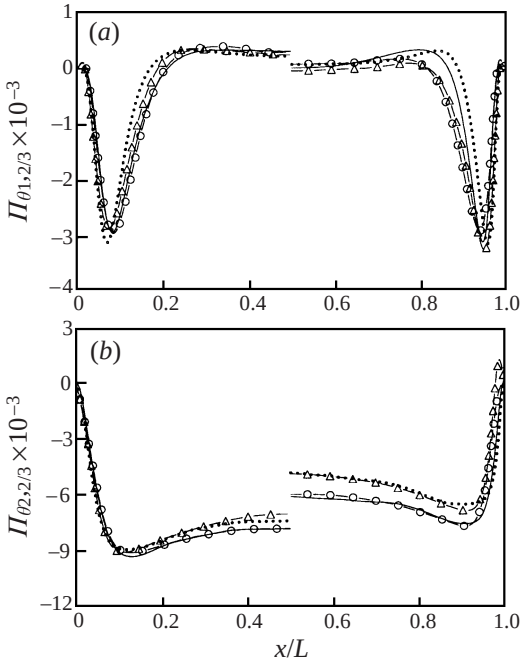

FIGURE 15. The performance of the new rapid/buoyant model at several Rayleigh numbers. For $x/L < 0.5$: model (—, $Ra = 5.4\times10^5$; ···, $Ra = 8.227\times10^5$) evaluated/compared with DNS (–○–, $Ra = 5.4\times10^5$; –△–, $Ra = 8.227\times10^5$). For $x/L > 0.5$: model (—, $Ra = 2\times10^6$; ···, $Ra = 5\times10^6$) evaluated/compared with DNS (–○–, $Ra = 2\times10^6$; –△–, $Ra = 5\times10^6$).

is relatively small, as shown by DNS data for $Ra = 5.4\times10^5$ in figure 16, together with the sum of the other parts.

The models that are available in the literature often implement a wall correction either to parts of or to the total $\Pi_{\theta i}$. Discriminatory suppression of the component perpendicular to the wall is achieved using the wall distance and the wall unit normal n_i. In principle, this approach can be tuned for simple plane walls; nevertheless, comparison with the DNS data shows that all available models perform poorly. For illustration, we have evaluated from DNS data the basic model proposed by Gibson & Launder 1978 (only for the slow term):

$$\hat{\Pi}^{\mathrm{w}}_{\theta i,1} = c^{\mathrm{w}}_{1\theta}\hat{\Pi}_{\theta j,1} f_{\mathrm{w}} n_j n_i, \tag{3.25}$$

$$f_{\mathrm{w}} = \min\left[\sum_{\mathrm{walls}} \frac{k^{3/2}}{c_{\mathrm{w}}\varepsilon x_{\mathrm{n}}}, 1.4\right], \tag{3.26}$$

where $c^{\mathrm{w}}_{1\theta} = 0.2$ and $c_{\mathrm{w}} = 2.53$, after Peeters & Henkes (1992). The function f_{w} is the one from Hanjalić *et al.* (1997*b*). We found that the upper bound is necessary for obtaining converged simulation results for the vertical channel. Actually, f_{w} will exceed the upper limit everywhere except close to the walls where it goes to zero. Originally, the function was designed in conjunction with wall functions to be unity near a wall (but outside the viscous layer) and decreasing to zero when moving away from it. This behaviour is clearly not suited for integration up to the wall when dealing with natural convection. The elliptic relaxation method, proposed by Durbin

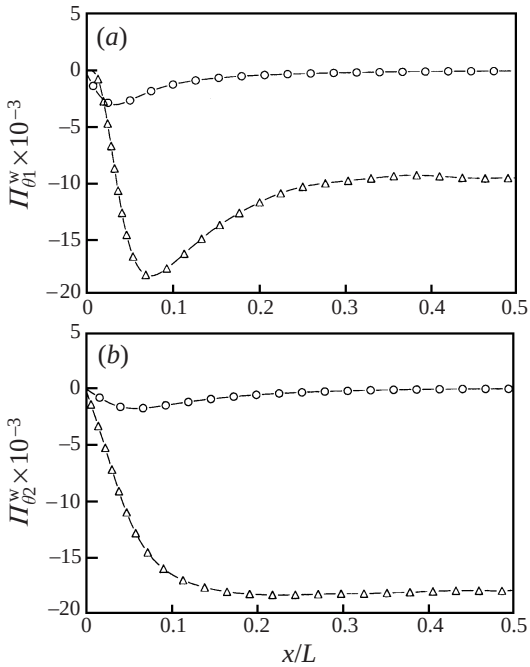

FIGURE 16. The wall-reflection part $\Pi^{w}_{\theta i}$ (–◯–) at $Ra = 5.4 \times 10^5$ for $i = 1$ (a) and $i = 2$ (b) compared with the sum of the slow, rapid and buoyant parts (–△–).

(1993), may eliminate the need for topological parameters, but it requires the solution of additional differential equations for damping functions for each stress and heat flux component.

Equation (3.25) yields zero $\Pi^{w}_{\theta i}$ for the vertical component and a negligible term for the horizontal component, as was shown by Dol *et al.* (1997). In order to eliminate the topology-dependent parameters in a relatively simple way, while improving the reproduction of $\Pi^{w}_{\theta i}$ for both components, we devised the following model:

$$\hat{\Pi}^{w}_{\theta i} = c^{w}_{\theta}|a_{ij}|(\hat{\Pi}_{\theta j,1} + \hat{\Pi}_{\theta j,2/3}), \tag{3.27}$$

$$c^{w}_{\theta} = \max(0, 0.58 - 0.69A^{1/2}), \tag{3.28}$$

where the stress-anisotropy tensor is used to differentiate between the horizontal and vertical components. As shown by figure 17, we were not able to match entirely the DNS data at $Ra = 5.4 \times 10^5$ for the horizontal component in the near-wall region without increasing significantly the model complexity. However, due to the relatively small magnitude of the wall term, the error will be small. Figure 18 shows good performance of the new wall model at all four Rayleigh numbers.

3.4.4. *The complete model for pressure scrambling*

As illustrated above, excellent reproduction of DNS results was achieved for all parts of $\Pi_{\theta i}$, but what really counts is the performance of the complete model. We recall here that $\hat{\Pi}_{\theta i} = \hat{\Pi}_{\theta i,1} + \hat{\Pi}_{\theta i,2} + \hat{\Pi}_{\theta i,3} + \hat{\Pi}^{w}_{\theta i,1}$ for the basic model and $\hat{\Pi}_{\theta i} = \hat{\Pi}_{\theta i,1} + \hat{\Pi}_{\theta i,2/3} + \hat{\Pi}^{w}_{\theta i}$ for the present new models. Not surprisingly, the errors in the new models are mainly caused by the slow part, see figures 8 and 19 for $Ra = 5.4 \times 10^5$.

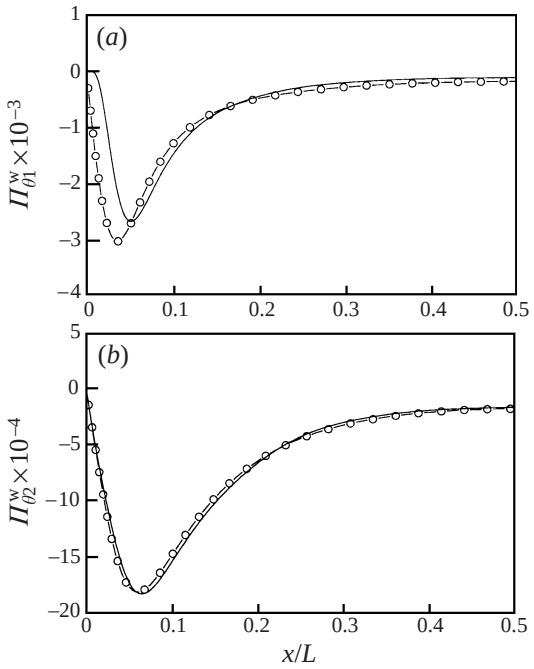

FIGURE 17. The performance of the new wall-reflection model (—; –◯–, DNS) at $Ra = 5.4 \times 10^5$ for $i = 1$ (*a*) and $i = 2$ (*b*).

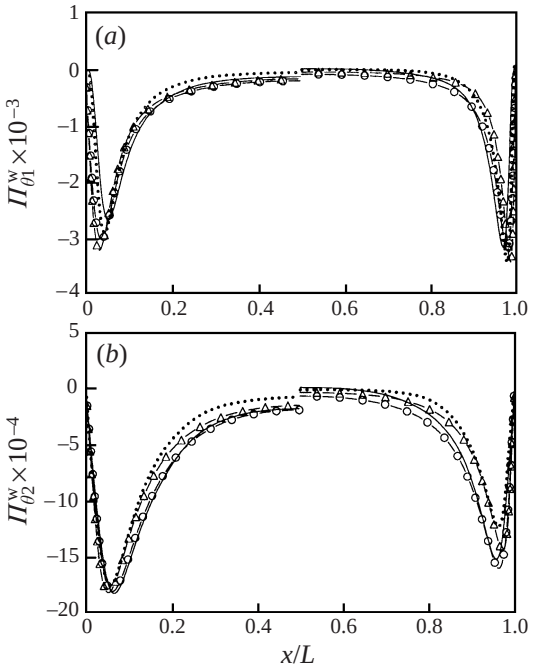

FIGURE 18. The performance of the new wall model at several Rayleigh numbers. For an explanation of the lines and symbols, see figure 15.

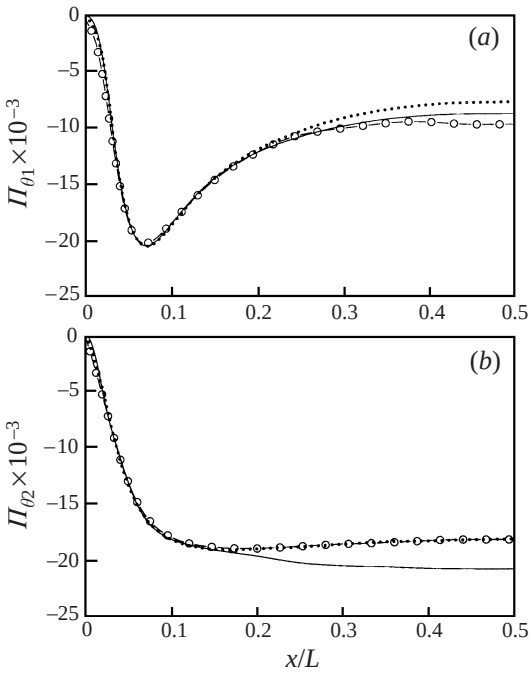

FIGURE 19. The performance of the new pressure-scrambling models (—, using quadratic slow model; ···, using cubic slow model; –◯–, DNS) at $Ra = 5.4 \times 10^5$ for $i = 1$ (a) and $i = 2$ (b).

Compared with the basic model, shown in figure 20, the new models perform very well with both slow models. Figure 20 also displays the model of Craft, Graham & Launder (1993) (their model 4) which performs somewhat better than the basic model, but is still far from the DNS data. The extra term proportional to the mean temperature gradient is certainly not negligible for the present flow, especially for $i = 2$ where it almost doubles its share in the slow model. The other component benefits slightly by including the extra term.

Figure 21 shows the performance of the new models at all available Rayleigh numbers. The predictions for all cases are satisfactory, particularly in the near-wall region, which is the target of the present study. Small inconsistencies are noticeable in the central region at the highest two Rayleigh numbers, where the quadratic model performs best for the vertical component and the cubic model for the horizontal component. Depending on the models for the other budget terms and the models for the velocity field, one or the other choice may be preferred, but the difference is not expected to produce much effect and is believed to be insignificant in the prediction of the mean-flow properties.

4. Simulations with the new thermal model

The new thermal second-moment closure, denoted by DH, is defined by equations (3.9), (3.10), (last term omitted), (3.11), (3.13), (3.19) (quadratic and cubic), (3.22), (3.27) and $R = 0.5$. It will be compared with the basic-model implementation of Peeters & Henkes (1992), denoted by PH. The thermal models are implemented in a standard finite-volume numerical code, together with the mechanical model of Hanjalić, Jakirlić & Hadžić (1997*a*), denoted by JH, listed in the Appendix.

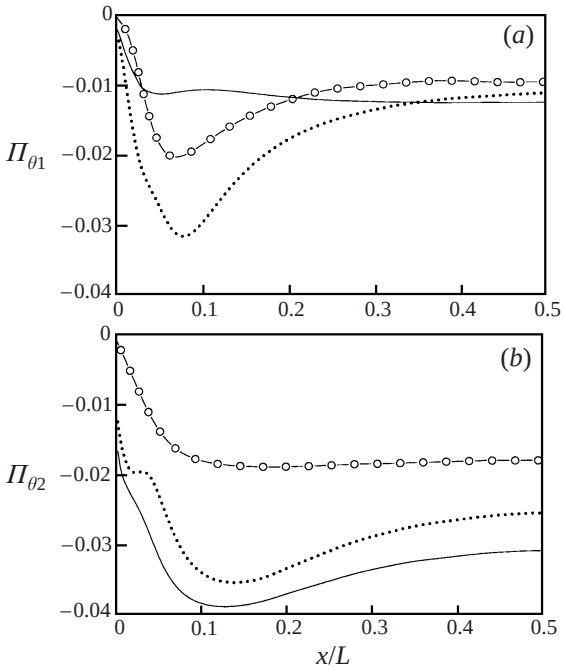

FIGURE 20. The performance of the basic model (—) and the model of Craft *et al.* (1993) (···; –◯–, DNS) at $Ra = 5.4 \times 10^5$ for $i = 1$ (*a*) and $i = 2$ (*b*).

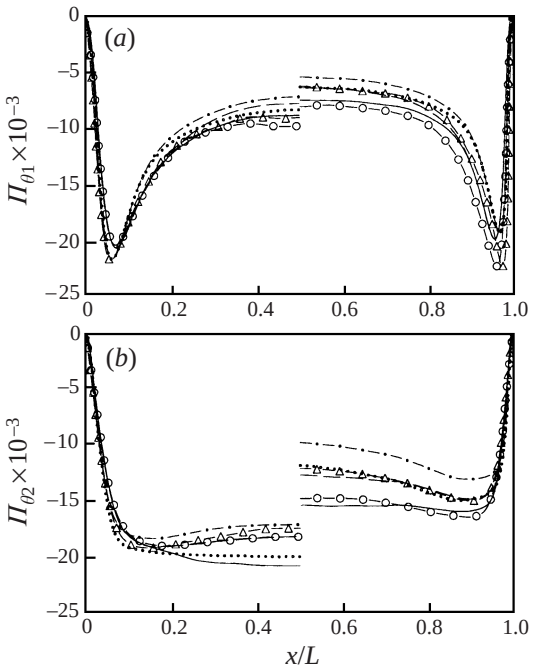

FIGURE 21. The performance of the new pressure-scrambling model at several Rayleigh numbers. For an explanation of the lines and symbols, see figure 12.

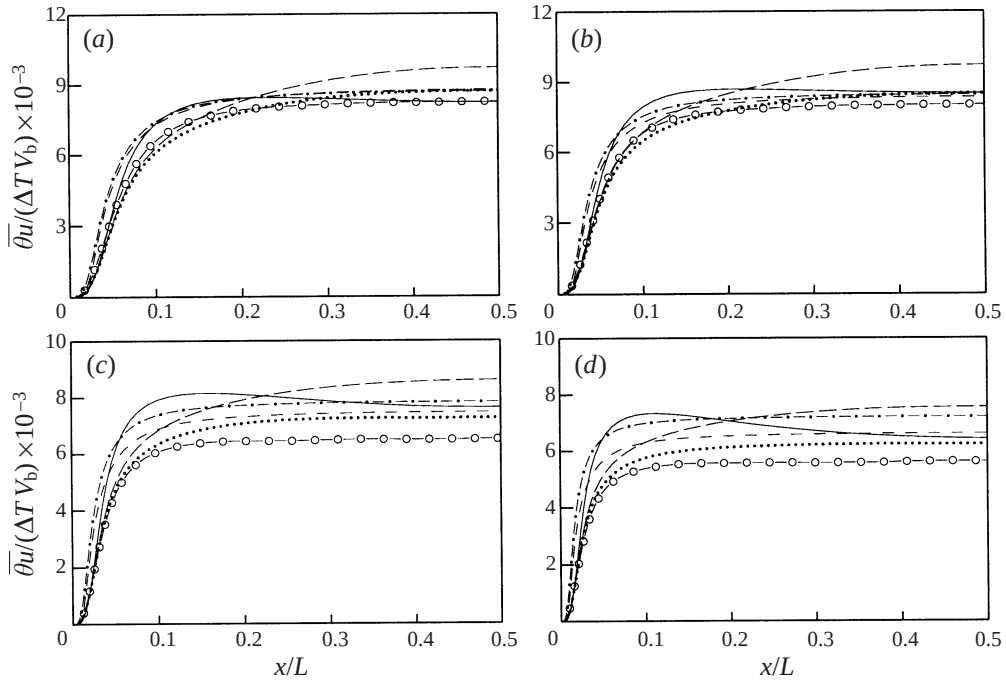

FIGURE 22. The horizontal heat flux at $Ra = 5.4 \times 10^5$ (*a*), $Ra = 8.227 \times 10^5$ (*b*), $Ra = 2 \times 10^6$ (*c*) and $Ra = 5 \times 10^6$ (*d*). The modelling results (—, PH+DNS; · · ·, DH1+DNS; – –, DH2+DNS; –·–, PH+JH; - - -, DH1+JH) are compared with the DNS data (–○–).

Simulations are then performed to test the abilities of the different models to predict the turbulent heat flux and temperature variance, compared with the DNS data.

The numerical code solves the discretized versions of the equations for the vertical velocity component V, temperature T, turbulent kinetic energy k, its dissipation rate ε, Reynolds stresses $\overline{u^2}$, $\overline{v^2}$ and $\overline{uv}$, turbulent heat fluxes $\overline{\theta u}$ and $\overline{\theta v}$ and temperature variance $\overline{\theta^2}$. Grid-independent solutions were obtained using a numerical grid consisting of 100 grid points, clustered near the wall. Although a set of 10 coupled transport equations has to be solved, due to the absence of convection terms each simulation takes only about one minute of CPU time on a HP-9000/735 workstation equipped with a single HPPA-7200 (125 MHz) processor. The simulations start from a reasonably good initial field, such as DNS data, or a previous simulation at a different Rayleigh number or with a different model.

Figures 22–24 show the predictions for the turbulent heat flux and the temperature variance at all four Rayleigh numbers. In order to quantify the influence of the mechanical model on the performance of the complete model, simulations are also made without the mechanical model. In that case, only the equations for $\overline{\theta u}$, $\overline{\theta v}$ and $\overline{\theta^2}$ are solved while the other variables are frozen at the DNS values interpolated on the numerical grid. These simulations are denoted in the figures by PH+DNS (basic model), DH1+DNS (model 1) and DH2+DNS (model 2). The full simulations, in which the transport equations for all variables are solved, are denoted by PH+JH (basic model) and DH1+JH (model 1). Model 2 in combination with the model of Hanjalić *et al.* (1997*a*) posed some convergence problems, whereas model 1 proved to be almost equally as robust as the basic model. In view of the fact that various complex and mathematically rigorous models, proposed in literature, are usually very difficult

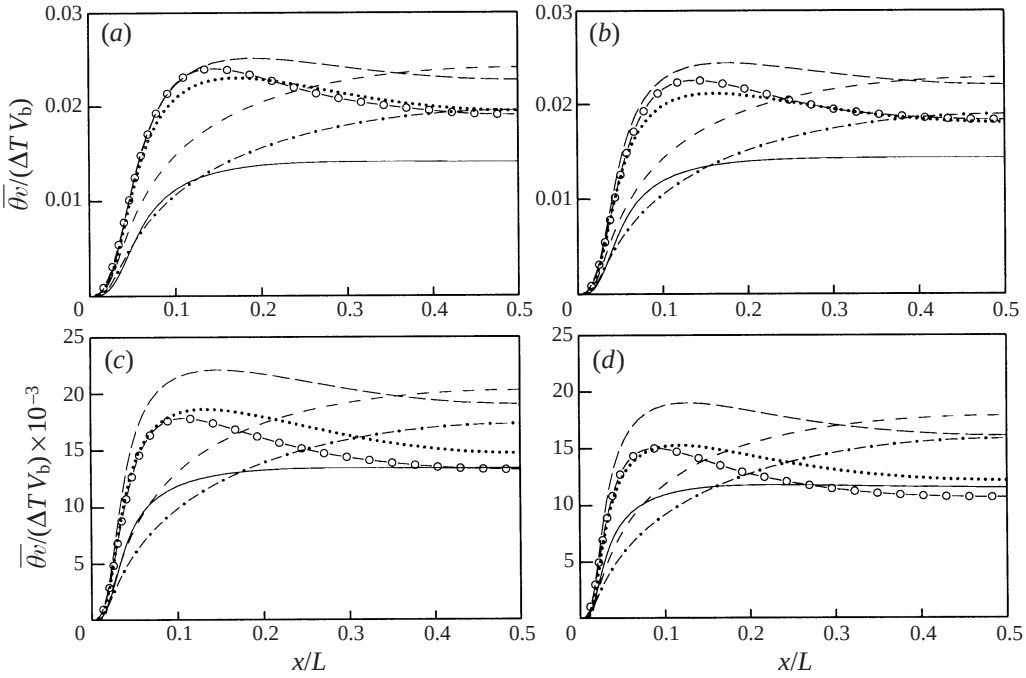

FIGURE 23. Similar to figure 22, but for the vertical heat flux.

to use in flows less trivial than the homogeneous turbulence for which they have been derived, the numerical robustness of model 1 is a very useful feature, opening prospects for the computation of buoyancy-driven flows of industrial relevance. The higher numerical stability of the quadratic model eventually makes it preferable to the cubic model. The full simulation with model 1 at $Ra = 5.4 \times 10^5$, started from the DNS field, took approximately 5.4 ms per iteration, which is only 20% longer than with the basic model. However, due to the fact that the new model requires heavier under-relaxation, more iterations are needed to reach the convergence criterion, increasing the total execution time by approximately 70%.

Figures 22(*a*), 23(*a*) and 24(*a*) show that the major defects of the basic model have been eliminated with model 1: the peaks in the profiles for $\overline{\theta v}$ and $\overline{\theta^2}$ are now closely reproduced. However, it is evident that the influence of the mechanical model on the thermal variables is significant. At present the effect of buoyancy on the stress field has been introduced only through the buoyancy production in both the stress and dissipation equations, but that proved to be insufficient for obtaining predictions of equally good quality as in *a priori* computations. The mechanical model, which was optimized for a range of isothermal shear flows, has to be further extended to account for the thermal effect on turbulence in the near-wall region, particularly in the near-wall modification of the coefficients in the modelled pressure–strain term. This task is left for future research.

Figures 22–24 show that the advantages of the new model are also convincing for the higher Rayleigh numbers. Only the magnitude of the temperature variance increases significantly with *Ra*. The origin of this discrepancy is in the Rayleigh-number dependence of the thermal-to-mechanical time-scale ratio *R*, which was kept constant in the present computations. The near-wall shape and slope of $\overline{\theta^2}$ agrees well with the DNS for all considered Rayleigh numbers and it is insensitive to the choice

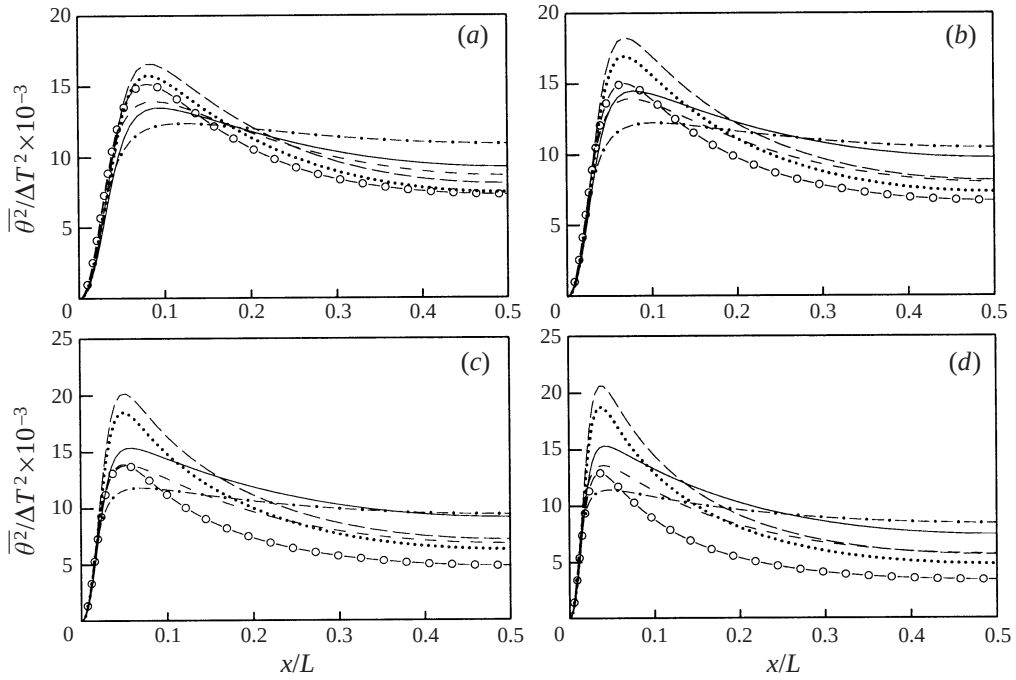

FIGURE 24. Similar to figure 22, but for the temperature variance.

of the thermal model or whether the mechanical model is applied. For the turbulent heat flux, the near-wall slope decreases below the DNS data when the mechanical model is activated. The same effect is noticed for the vertical component when the basic model is used instead of the new thermal models. Despite the fact that activating the mechanical model flattens the peaks of $\overline{\theta v}$ and $\overline{\theta^2}$, the space-averaged values are close to DNS for $Ra = 5.4 \times 10^5$ ($\overline{\theta v}$ and $\overline{\theta^2}$) and $Ra = 8.227 \times 10^5$ ($\overline{\theta v}$ only). For $\overline{\theta v}$, this does not hold when the basic model is used.

Dol *et al.* (1997) show that algebraic models that can be derived for the heat fluxes by neglecting or approximating transport, are not in themselves serious competitors to the differential model here derived. Only due to the dominant influence of the quantities for which transport equations are solved, do the resulting 'partial' algebraic models appear perform comparably to the differential basic model. These observations stress the importance of solving thermal transport equations equipped with accurate near-wall models, but also indicate a need to implement the effects of buoyancy in the mechanical model, which is the 'backbone' even for a thermally-driven flow.

5. Conclusions

Direct Numerical Simulations of a thermally driven flow between two infinite vertical plates have been analysed focusing on the behaviour and scaling of second thermal moments and their budget in the near-wall and central channel regions. The data revealed some interesting features which distinguish the thermally driven flows from the forced isothermal flows in similar configurations. A major difference appears in the multiple production of the turbulent stress (mean shear and buoyancy) and of the heat flux (mean shear, mean temperature gradient and buoyancy), which are all of the same order of magnitude. Also, the mechanical production (mean shear) is

negative close to the wall for all second moments (changing sign around the mean velocity maximum) whereas all stress and flux components are everywhere positive (except for a negligible negative shear stress very close to the wall). All these findings invalidate linear eddy-viscosity and eddy-diffusivity assumptions, indicating a need to employ the second-moment closure approach as a minimum modelling level. Another important feature is that the major sink of the turbulent heat flux is the pressure scrambling, whereas the molecular dissipation is negligible, except very close to the wall where it balances molecular transport. A striking difference in comparison with the stress budget in a plane channel is that the return-to-isotropy (slow) term is the dominant constituent of the pressure-scrambling process for all heat-flux components as well as for all stresses, except for the shear stress where the rapid term is the largest.

Based on the DNS of turbulent natural convection in a differentially heated vertical channel, a differential thermal second-moment closure has been developed. The model approximates all separate unclosed budget terms of the transport equations for the turbulent heat flux and temperature variance very well, especially in the important near-wall region. It contains no wall distances nor wall normals and is thus suitable for general flows bounded by walls of complex topologies. The DNS data at the lowest available Rayleigh number (5.4×10^5) have been used for model calibration, but the model is shown to reproduce almost equally well the flows at other Rayleigh numbers (up to 5×10^6). The new thermal model proves to be a major improvement when compared with the current practice (e.g. the thermal part of the basic model). Major advantages are the very satisfactory term-by-term prediction of budgets for the heat flux and temperature variance and exclusive use of local flow and turbulence parameters allowing complex wall topology. All these improvements are achieved with a marginal increase in model complexity which makes no special demands on model implementation into general computer codes.

However, the true generality of the model can only be proved when successfully applied to different types of problems, for example Rayleigh–Bénard convection, or to flows in more complex domains. Another weakness is the mechanical model: the present research indicated that the advantages of the thermal model are diminished when used together with the existing mechanical models, which have not been well tested in thermally driven flows. This is an urgent task, which was beyond the scope of present investigation. It is believed, however, that the available DNS database and principles adopted in the present work in modelling the heat flux and temperature variance can serve as a guidance for improvement of the modelling of buoyancy effects on the mechanical turbulence.

This research was supported by the Dutch Foundation for Fundamental Research on Matter (FOM) with financial aid from the Dutch Technology Foundation (STW).

Appendix. The mechanical second-moment closure

This Appendix summarizes the differential second-moment closure of Hanjalić *et al.* (1997*a*) with the addition of buoyancy terms (production and pressure strain). Developed and optimized for a range of equilibrium and non-equilibrium attached and separating isothermal flows, it only provides a closure of the transport equations for the Reynolds stress $\overline{u_i u_j}$ and the energy dissipation rate. In the present study, this mechanical model is used together with the (new) thermal model in order to close the complete set of equations.

The exact equation for $\overline{u_i u_j}$ is

$$\frac{\mathrm{D}\overline{u_i u_j}}{\mathrm{D}t} = \underbrace{\frac{\partial}{\partial x_k}\left[\underbrace{\nu\frac{\partial \overline{u_i u_j}}{\partial x_k}}_{\mathscr{D}^{\nu}_{ij}} \boxed{\underbrace{-\overline{u_i u_j u_k}}_{\mathscr{D}^{\mathrm{t}}_{ij}}}\right]}_{\mathscr{D}_{ij}} \underbrace{-\left(\overline{u_i u_k}\frac{\partial U_j}{\partial x_k} + \overline{u_j u_k}\frac{\partial U_i}{\partial x_k}\right)}_{P_{ij}}$$

$$\boxed{\underbrace{-(g_i\beta\overline{\theta u_j} + g_j\beta\overline{\theta u_i})}_{G_{ij}}} \boxed{\underbrace{-\left(\overline{\frac{\partial p}{\partial x_i}\frac{u_j}{\rho}} + \overline{\frac{\partial p}{\partial x_j}\frac{u_i}{\rho}}\right)}_{\Pi_{ij}}} - \boxed{\underbrace{2\nu\overline{\frac{\partial u_i}{\partial x_k}\frac{\partial u_j}{\partial x_k}}}_{\varepsilon_{ij}}} \tag{A 1}$$

where the terms in boxes require modelling.

As the pressure diffusion $\mathscr{D}^{p}_{ij} = -(\partial\overline{pu_j}/\partial x_i + \partial\overline{pu_i}/\partial x_j)/\rho$ is not modelled separately, the model for the total pressure term $\Pi_{ij} = \Phi_{ij} + \mathscr{D}^{p}_{ij}$ is assumed to retain the redistributive character:

$$\hat{\Pi}_{ij} = \hat{\Pi}_{ij,1} + \hat{\Pi}_{ij,2} + \hat{\Pi}_{ij,3} + \hat{\Pi}^{\mathrm{w}}_{ij,1} + \hat{\Pi}^{\mathrm{w}}_{ij,2}, \tag{A 2}$$

$$\hat{\Pi}_{ij,1} = -c_1\varepsilon a_{ij}, \tag{A 3}$$

$$\hat{\Pi}_{ij,2} = -c_2(P_{ij} - \tfrac{1}{3}P_{kk}\delta_{ij}), \tag{A 4}$$

$$\hat{\Pi}_{ij,3} = -c_3(G_{ij} - \tfrac{1}{3}G_{kk}\delta_{ij}), \tag{A 5}$$

$$\hat{\Pi}^{\mathrm{w}}_{ij,1} = c^{\mathrm{w}}_1\frac{\varepsilon}{k}(\overline{u_k u_l}n_k n_l\delta_{ij} - \tfrac{3}{2}\overline{u_i u_k}n_k n_j - \tfrac{3}{2}\overline{u_j u_k}n_k n_i)f_{\mathrm{w}}, \tag{A 6}$$

$$\hat{\Pi}^{\mathrm{w}}_{ij,2} = c^{\mathrm{w}}_2(\hat{\Pi}_{kl,2}n_k n_l\delta_{ij} - \tfrac{3}{2}\hat{\Pi}_{ik,2}n_k n_j - \tfrac{3}{2}\hat{\Pi}_{jk,2}n_k n_i)f_{\mathrm{w}}, \tag{A 7}$$

$$f_{\mathrm{w}} = \min\left[\sum_{\mathrm{walls}}\frac{k^{3/2}}{c_{\mathrm{w}}\varepsilon x_{\mathrm{n}}}, 1.4\right]. \tag{A 8}$$

The constants are given in table 6. Modifications for the near-wall proximity and satisfying the two-component limit are achieved by expressing the coefficients as functions of invariant turbulence parameters: the turbulence Reynolds number (viscous effects), stress invariants A_2, A_3 and A, and their analogues for the stress-dissipation tensor ε_{ij}, i.e. E_2, E_3 and E:

$$c_1 = c + \sqrt{A}E^2, \quad c_3 = c_2 = 0.8\sqrt{A}, \tag{A 9), (A 10}$$

$$c^{\mathrm{w}}_1 = \max(1 - 0.7c, 0.3), \quad c^{\mathrm{w}}_2 = \min(A, 0.3), \quad c = 2.5AF^{1/4}f, \tag{A 11), (A 12), (A 13}$$

$$F = \min(0.6, A_2), \quad f = \min\left[\left(\frac{Re_{\mathrm{t}}}{150}\right)^{3/2}, 1\right], \tag{A 14), (A 15}$$

$$Re_{\mathrm{t}} = k^2/\nu\varepsilon. \tag{A 16}$$

Sufficiently far away from a wall, the functions take constant values that are close to the typical high-Re_{t} values from the literature. However, in the near-wall region, where the turbulent Reynolds number Re_{t} is relatively low and the anisotropy high, the functions will become effective.

$c_{\overline{u_iu_j}}$	c_w	c_ε	$c_{\varepsilon1}$	$c_{\varepsilon2}$	$c_{\varepsilon3}$	c'_ε
0.22	2.5	0.18	1.44	1.92	1	0.125

TABLE 6. The constants of the mechanical model.

The model for the stress-dissipation rate is based on the homogeneous–inhomogeneous decomposition the homogeneous part of which $\varepsilon\overline{u_iu_j}/k$ is modified to obtain the correct near-wall behaviour:

$$-\hat{\varepsilon}_{ij} = -(1-f_s)\tfrac{2}{3}\varepsilon\delta_{ij} - f_s\varepsilon^*_{ij}, \tag{A 17}$$

$$-\varepsilon^*_{ij} = -\frac{\varepsilon}{k}\frac{\overline{u_iu_j} + (\overline{u_iu_k}n_kn_j + \overline{u_ju_k}n_kn_i + \overline{u_ku_l}n_kn_in_in_j)f_d}{1+\frac{3}{2}(\overline{u_lu_m}/k)n_ln_mf_d}, \tag{A 18}$$

$$f_s = 1-\sqrt{A}E^2, \quad f_d = \frac{1}{1+\frac{1}{10}Re_t}. \tag{A 19), (A 20}$$

A rationale for this model and illustrations of its performance in equilibrium and separated flows are provided by Hanjalić & Jakirlić (1993) and Hanjalić *et al.* (1997*a*).

The exact equation for $\varepsilon = \frac{1}{2}\varepsilon_{kk}$ can be written as

$$\frac{\mathrm{D}\varepsilon}{\mathrm{D}t} = \underbrace{\frac{\partial}{\partial x_k}\left[\underbrace{\nu\frac{\partial\varepsilon}{\partial x_k}}_{\mathscr{D}^v_\varepsilon}\boxed{\underbrace{-\overline{\varepsilon' u_k}}_{\mathscr{D}^t_\varepsilon}}\boxed{\underbrace{-\frac{2\nu}{\rho}\overline{\frac{\partial p}{\partial x_l}\frac{\partial u_k}{\partial x_l}}}_{\mathscr{D}^p_\varepsilon}}\right]}_{\mathscr{D}_\varepsilon}\boxed{\underbrace{-\varepsilon_{kl}\frac{\partial U_k}{\partial x_l}}_{P^1_\varepsilon}}$$
$$\boxed{\underbrace{-2\nu\overline{\frac{\partial u_m}{\partial x_k}\frac{\partial u_m}{\partial x_l}}\frac{\partial U_k}{\partial x_l}}_{P^2_\varepsilon}}\boxed{\underbrace{-2\nu u_k\overline{\frac{\partial u_m}{\partial x_l}\frac{\partial^2 U_m}{\partial x_k\partial x_l}}}_{P^3_\varepsilon}}$$
$$\boxed{\underbrace{-\varepsilon'_{kl}\overline{\frac{\partial u_k}{\partial x_l}}}_{P^4_\varepsilon}}\boxed{\underbrace{-\frac{2\nu}{\nu+\alpha}g_k\beta\varepsilon_{\theta k}}_{G_\varepsilon}}-\boxed{\underbrace{2\overline{\left(\nu\frac{\partial^2 u_m}{\partial x_k\partial x_l}\right)^2}}_{Y}} \tag{A 21}$$

where $\varepsilon'_{ij} = 2\nu(\partial u_i/\partial x_k)(\partial u_j/\partial x_k)$ and $\varepsilon' = \frac{1}{2}\varepsilon'_{kk}$ and with wall boundary condition $\varepsilon_w = 2\nu(\partial k^{1/2}/\partial x_n)^2_w$. Again, the terms in boxes require modelling.

The only other term that is modelled separately is P^3_ε, applying the Daly & Harlow gradient-diffusion hypothesis for $\overline{u_k(\partial u_m/\partial x_l)}$:

$$\hat{P}^3_\varepsilon = 2\nu c'_\varepsilon\frac{k}{\varepsilon}\overline{u_ku_n}\frac{\partial^2 U_m}{\partial x_l\partial x_n}\frac{\partial^2 U_m}{\partial x_k\partial x_l}. \tag{A 22}$$

As in the standard k-ε model, all the other unclosed terms are lumped together and

modelled jointly:

$$\hat{P}_\varepsilon^1 + \hat{P}_\varepsilon^2 + \hat{P}_\varepsilon^4 + \hat{G}_\varepsilon - \hat{Y} = c_{\varepsilon 1}(P_{kk} + c_{\varepsilon 3} G_{kk})\frac{\varepsilon}{2k} - c_{\varepsilon 2} f_\varepsilon \frac{\tilde{\varepsilon}\varepsilon}{k}, \tag{A 23}$$

$$f_\varepsilon = 1 - \frac{c_{\varepsilon 2} - 1.4}{c_{\varepsilon 2}} \exp\left[-\left(\frac{Re_t}{6}\right)^2\right], \tag{A 24}$$

$$\tilde{\varepsilon} = \varepsilon - 2\nu\left(\frac{\partial k^{1/2}}{\partial x_k}\right)^2. \tag{A 25}$$

Equal weight of shear and buoyant production is assumed, which was found appropriate for natural convection along heated/cooled vertical walls. The modelled equation contains two more invariant terms, which are not shown, to enhance the irrotational-strain production and to suppress the excessive scale growth in non-equilibrium flows, which are considered as unimportant for the present flow problem.

The turbulent velocity diffusion is modelled in both transport equations using the Daly & Harlow expression:

$$\hat{\mathscr{D}}_\phi^t = \frac{\partial}{\partial x_k}\left[c_\phi \frac{k}{\varepsilon}\overline{u_k u_l}\frac{\partial \phi}{\partial x_l}\right] \tag{A 26}$$

where ϕ stands for $\overline{u_i u_j}$ and ε, respectively.

REFERENCES

Balachandar, S., Maxey, M. R. & Sirovich, L. 1989 Numerical simulation of high Rayleigh number convection. *J. Sci. Comput.* **4**, 219–236.

Boudjemadi, R., Maupu, V., Laurence, D. & Le Quéré, P. 1997 Budgets of turbulent stresses and fluxes in a vertical slot natural convection at Rayleigh $Ra = 10^5$ and 5.4×10^5. *Intl J. Heat Fluid Flow* **18**, 70–79.

Craft, T. J., Graham, L. J. W. & Launder, B. E. 1993 Impinging jet studies for turbulence model assessment–II. An examination of the performance of four turbulence models. *Intl J. Heat Mass Transfer* **36**, 2685–2697.

Craft, T. J. & Launder, B. E. 1989 A new model for the pressure/scalar-gradient correlation and its application to homogeneous and inhomogeneous free shear flows. *Proc. 7th Symp. Turb. Shear Flows, Stanford, CA, USA.*

Dol, H. S., Hanjalić, K. & Kenjereš, S. 1997 A comparative assessment of the second-moment differential and algebraic models in turbulent natural convection. *Intl J. Heat Fluid Flow* **18**, pp. 4–14.

Daly, B. J. & Harlow, F. H. 1970 Transport equations in turbulence. *Phys. Fluids* **13**, pp. 2634–2649.

Durbin, P. A. 1993 A Reynolds stress model without for near wall turbulence. *J. Fluid Mech.* **249**, 465–498.

Gibson, M. M. & Launder, B. E. 1978 Ground effects on pressure fluctuations in the atmospheric boundary layer. *J. Fluid Mech.* **86**, 491–511.

Girimaji, S. S. & Balachandar, S. 1997 Analysis and modelling of buoyancy generated turbulence using numerical data. *Intl J. Heat Mass Transfer* **41**, 915–929.

Groth, J. 1991 Description of the pressure effects in the Reynolds stress transport equations. *Phys. Fluids* A **3**, 2276–2277.

Grötzbach, G. 1982 Direct numerical simulation of laminar and turbulent Bénard convection. *J. Fluid Mech.* **119**, 27–53.

Grötzbach, G. 1983 Spatial resolution requirements for direct numerical simulation of Rayleigh-Bénard convection. *J. Comput. Phys* **49**, 241–246.

Hanjalić, K. & Jakirlić, S. 1993 A model of stress dissipation in second-moment closures. *Appl. Sci. Res.* **51**, 513–518.

Hanjalić, K., Jakirlić, S. & Hadžić, I. 1997*a* Expanding the limits of 'equilibrium' second-moment turbulence closures. *Fluid Dyn. Res.* **20**, 25–41.

Hanjalić, K., Jakirlić, S. & Ristorcelli, J. R. 1997*b* Alternative approach to modelling the dissipation equation. *Advances in Turbulence VI* (ed. S. Gavrilakis *et al.*), pp. 27–30. Kluwer.

Hanjalić, K. & Launder, B. E. 1972 A Reynolds stress model of turbulence and its application to thin shear flows. *J. Fluid Mech.* **52**, 609–638.

Hanjalić, K. & Vasić, S. 1993 Some further exploration of turbulence models for buoyancy driven flows. *Turbulent Shear Flows 8* (ed. F. Durst *et al.*), pp. 319–341. Springer.

Henkes, R. A. W. M. & Le Quéré, P. 1996 Three-dimensional transition of natural-convection flows. *J. Fluid Mech.* **319**, 281–303.

Jones, W. P. & Musonge, P. 1983 Modelling of scalar transport in homogeneous turbulent flows. *Proc. 4th Symp. Turb. Shear Flows, Karlsruhe, Germany.*

Jones, W. P. & Musonge, P. 1988 Closure of the Reynolds stress and scalar flux equations. *Phys. Fluids* **31**, 3589–3604.

Kenjereš, S. & Hanjalić, K. 1995 Prediction of turbulent thermal convection in concentric and eccentric annuli. *Intl J. Heat Fluid Flow* **16**, 428–439.

Launder, B. E. 1989 Second-moment closure: present ... and future? *Intl J. Heat Fluid Flow* **10**, 282–300.

Launder, B. E., Reece, G. J. & Rodi, W. 1975 Progress in the development of a Reynolds-stress turbulence closure. *J. Fluid Mech.* **68**, 537–566.

Launder, B. E. & Tselepidakis, D. P. 1991 Progress and paradoxes in modelling near-wall turbulence. *Proc. 8th Symp. Turb. Shear Flows, Munich, Germany.*

Lipps, F. B. 1976 Numerical simulation of three-dimensional Bénard convection in air. *J. Fluid Mech.* **75**, 113–148.

Lumley, J. L. 1975 Pressure-strain correlation. *Phys. Fluids* **18**, 750.

Lumley, J. L. 1978 Computational modelling of turbulent flows. *Adv. Appl. Mech.* **18**, 123–176.

Lumley, J. L. & Newman, G. R. 1977 The return to isotropy of homogeneous turbulence. *J. Fluid Mech.* **82**, 161–178.

Mansour, N. N., Kim, J. & Moin, P. 1988 Reynolds-stress and dissipation-rate budgets in a turbulent channel flow. *J. Fluid Mech.* **194**, 15–44.

Monin, A. S. & Yaglom, A. M. 1975 *Statistical Fluid Mechanics: Mechanics of Turbulence* (ed. J. L. Lumley), Vol. 2. MIT Press.

Paolucci, S. 1990 Direct numerical simulation of two-dimensional turbulent natural convection in an enclosed cavity. *J. Fluid Mech.* **215**, 229–262.

Peeters, T. W. J. & Henkes, R. A. W. M. 1992 The Reynolds-stress model of turbulence applied to the natural-convection boundary layer along a heated vertical plate. *Intl J. Heat Mass Transfer* **35**, 403–420.

Shih, T.-H., Lumley, J. L. & Chen, J.-Y. 1988 Second-order modelling of a passive scalar in a turbulent shear flow. *AIAA J.* **28**, 610–617.

Shima, N. 1995 Modelling of asymptotic near-wall behaviour of the Reynolds stress dissipation. *Proc. 10th Symp. Turb. Shear Flows, Pennsylvania State University, USA.*

Speziale, C. G., Sarkar, S. & Gatski, T. B. 1991 Modelling the pressure-strain correlation on turbulence: an invariant dynamic system approach. *J. Fluid Mech.* **227**, 245–272.

Tavoularis, S. & Corrsin, S. 1985 Effects of shear on the turbulent diffusivity tensor. *Intl J. Heat Mass Transfer* **28**, 265–276.

Versteegh, T. A. M. 1998 Numerical simulation of natural convection in a differentially-heated vertical channel. PhD thesis, Delft University of Technology, Delft, The Netherlands.

Versteegh, T. A. M. & Nieuwstadt, F. T. M. 1997 Turbulent budgets of natural convection in an infinite, differentially heated, vertical channel. *Intl J. Heat Fluid Flow* **19**, 135–149.

Wörner, M. & Grötzbach, G. 1997 Pressure transport in DNS of turbulent natural convection in horizontal fluid layers. *Turbulence, Heat and Mass Transfer 2* (ed. K. Hanjalić & T. W. J. Peeters), pp. 351–360. Delft University Press.

Ye, Q. Y., Wörner, M., Grötzbach, G. & Jovanović, J. 1997 Modelling turbulent dissipation rate for Rayleigh-Bénard convection. *Turbulence, Heat and Mass Transfer 2*, (ed. K. Hanjalić & T. W. J. Peeters), pp. 331–340. Delft University Press.